

# Witnessing History: Rates and Detectability of Naked-Eye Milky-Way Supernovae

C. Tanner Murphey<sup>1,3,4</sup>, Jacob W. Hogan<sup>1,3,4</sup>, Brian D. Fields<sup>1,2,3,4</sup>, Gautham Narayan<sup>1,2,3,4</sup>

<sup>1</sup>Department of Astronomy, University of Illinois, Urbana, IL 61801

<sup>2</sup>Department of Physics, University of Illinois, Urbana, IL 61801

<sup>3</sup>Illinois Center for Advanced Studies of the Universe, University of Illinois, Urbana, IL 61801

<sup>4</sup>Center for Astrophysical Surveys, National Center for Supercomputing Applications, Urbana, IL, 61801, USA

Accepted XXX. Received YYY; in original form ZZZ

## ABSTRACT

The Milky Way hosts on average a few supernova explosions per century, yet in the past millennium only five supernovae have been identified confidently in the historical record. This deficit of naked-eye supernovae is at least partly due to dust extinction in the Galactic plane. We explore this effect quantitatively, developing a formalism for the supernova probability distribution, accounting for dust and for the observer’s flux limit. We then construct a fiducial axisymmetric model for the supernova and dust densities, featuring an exponential dependence on galactocentric radius and height, with core-collapse events in a thin disk and Type Ia events including a thick disk component. When no flux limit is applied, our model predicts supernovae are intrinsically concentrated in the Galactic plane, with Type Ia events extending to higher latitudes reflecting their thick disk component. We then apply a flux limit and include dust effects, to predict the sky distribution of historical supernovae. We use well-observed supernovae as light-curve templates, and introduce naked-eye discovery criteria. The resulting sky distributions are strikingly inconsistent with the locations of confident historical supernovae, none of which lie near our model’s central peaks. Indeed, SN 1054 lies off the plane almost exactly in the anticenter, and SN 1181 is in the 2nd Galactic quadrant. We discuss possible explanations for these discrepancies. We calculate the percentage of all supernovae bright enough for historical discovery:  $\approx 13\%$  of core-collapse and  $\approx 33\%$  of Type Ia events. Using these and the confident historical supernovae, we estimate the intrinsic Galactic supernova rates, finding general agreement with other methods. Finally, we urge searches for supernovae in historical records from civilizations in the southern hemisphere.

**Key words:** transients: supernovae, supernovae: general, supernovae: individual: SN 1006, SN 1054, SN 1181, SN 1572, SN 1604, Cassiopeia A

## 1 INTRODUCTION

A Galactic supernova (SN) has not been convincingly observed by the naked eye since Kepler’s SN 1604 (Kepler 1606). This 416 year gap is disappointing, and persists despite a long and fruitful effort to identify supernovae (SNe) in the historical record (e.g., Clark & Stephenson 1977; Stephenson & Green 2002, 2009). Over the four intervening centuries since Kepler’s event, modern Astronomy has arisen, bringing advancements in telescopes and observational techniques that should have, if anything, made it more likely that Galactic SNe would be noticed. Rates and observability of Galactic SNe are clearly worthy of investigation.

The important study of Adams, et al. (2013) anticipates the next Galactic SN, and uses historical data to estimate Galactic rates for both core-collapse and thermonuclear or Type Ia supernovae (hereafter CCSNe and SNIa, respectively). They conclude that the total rate of Galactic SNe corresponds to an average of one event per  $\sim 22$  years (Table 1). Based on previously predicted rates,  $\sim 18$  Galactic SNe should have occurred since Kepler’s. Other methods give Galactic SN rates that can vary by a factor  $\sim 2$  (Rozwadowska, Vissani, & Cappellaro 2021), but even within these uncertainties it is extremely

unlikely that no SN has occurred in the past 416 years. Of course, SNe preferentially occur within the Milky Way thin disk where dust is also concentrated, and so extinction will play an important role for distant events. It is thus widely acknowledged that *historic supernovae*—i.e., naked-eye events discernible in past records—should represent only a fraction of Galactic events; this is the subject of our study.

Observations of supernova remnants confirm that unseen events have occurred since Kepler. The Cassiopeia A remnant has a measured expansion age of about 325 years, corresponding to an explosion in  $1681 \pm 19$  (Fesen et al. 2006). It certainly was not widely observed; there have been claims that John Flamsteed saw it in 1680, but it is likely that he did not (Stephenson & Green 2005). As far as we know, the most recent Galactic supernova remnant (SNR) claimed in the literature is G1.9+0.3 with an age of about  $\sim 110 - 180$  yr, which places the explosion in the latter half of the 19th century (Luken, et al. 2019; Green & Gull 1984; Reynolds, et al. 2008). Thus, at least two Galactic supernovae have occurred since 1604.

To our knowledge, there are no remnants that are dated to be younger than G1.9+0.3, suggesting that there have been no Galactic events in the 20th or 21st centuries. During this time, technologies

have been developed to detect wavelengths invisible human eye in which the Galaxy is partly or entirely transparent: infrared, radio, and gamma-ray. Moreover, core-collapse events would be detected via neutrino monitoring that has been ongoing for around 40 years (Antonioli, et al. 2004; Ikeda et al. 2007; Novoseltsev et al. 2020; Scholberg 2012; DUNE collaboration et al. 2020; Al Kharusi et al. 2020), and now gravitational wave monitoring is provided by LIGO/VIRGO (Abbott et al. 2020). Type Ia events likely would escape these searches but would be found in gamma-ray burst monitors via their MeV line emission (Wang, Fields & Lien 2019). We can thus confidently look forward to witnessing the inevitable occurrence of the next Galactic supernova, with observations across much of the electromagnetic spectrum and possibly via other messengers. But the question remains as to how many were missed in the historical past, when the naked eye was the only available detector.

In this paper we study the naked-eye visibility of supernovae in our Galaxy, building in particular on the work of Adams, et al. (2013). In §2 we develop a general formalism to describe the supernova probability distribution in space and on the sky. This depends on the supernova spatial distribution, and we adopt axisymmetric models for this and for the Galactic dust distribution. In §3 we gather the information needed to assess the naked-eye visibility of Galactic supernovae. We use recent extragalactic supernova light curve data to assess the sustained luminosity of different supernova subtypes. We also model dust extinction effects, and review data on historical supernovae and present-day Galactic supernova rates. In §4 we present our model results, first showing sky maps of the intrinsic supernova probability on the sky. Then we show the sky distributions for naked-eye supernovae and compare them to the location historic events. We discuss in §5 the implications of the surprising comparison with historical data. We conclude in §6 by summarizing our results and suggesting future work.

## 2 GALACTIC SUPERNOVA DISTRIBUTIONS

### 2.1 Formalism

Our calculations are grounded in the spatial distribution of supernovae in the Galaxy. We develop a general formalism, but then construct a model that has three basic assumptions. The most drastic of these is that our Galaxy can be approximated as spatially axisymmetric, which means that we are ignoring the effects of both the central bar and spiral arms of the Milky Way galaxy. We also assume that both stars and dust can be characterized by exponential distributions in both height above the Galactic plane and radius from the central axis. Finally, we assume that over the timescales of interest the average rate of Galactic supernovae does not evolve; this is certainly the case for the historical period, where the larger uncertainty is due to the stochasticity of the precious few events for which we have records. We plan future work in which we relax some of these assumptions, but we also note that the are not uncommon and were also adopted by Adams, et al. (2013).

The fundamental quantity we use is the rate density  $q_i$  for supernova of type  $i$ :

$$\frac{dN_i}{dV dt} = q_i(R, z) \quad (1)$$

which gives the number of events per unit volume and time. Integrating the rate density over the entire volume gives the total Galactic rate of  $\mathcal{R}_i = \int q_i dV$  of supernovae of type  $i$ . We can go on to write

a probability distribution function,

$$\rho_i(R, z) = \frac{dP_i}{dV} = \frac{q_i(R, z)}{\mathcal{R}_i} \quad (2)$$

which gives the probability per unit volume of finding a supernova of type  $i$  at a point  $(R, z)$ . This probability density distribution is properly normalized, so that integrating over the Galactic volume gives  $\int \rho dV = 1$ . It also follows that we have  $q_i = \mathcal{R}_i \rho_i$ .

We will follow a common approach to modelling the Galactic disk components, approximating both radial and height density as exponential drop-offs. In this “double exponential” model, the disk component  $j$  has a normalized spatial probability distribution

$$\rho_j(R, z) = \frac{\exp(-R/R_j) \exp(-|z|/h_j)}{4\pi R_j^2 h_j} \quad (3)$$

where the two free parameters are the scale length  $R_j$  and scale height  $h_j$ . In this paper we will adopt distributions of this form, as did Adams, et al. (2013).

We start with our basic quantity: the supernova probability per unit area of the sky as seen from the Sun’s location at a Galactocentric radius and height of  $(R_\odot, z_\odot)$ . We use the observer’s Sun-centered Galactic (spherical) coordinates to calculate the supernova probability per solid angle, i.e., probability density per angular area. Namely, along a sightline in the  $(\ell, b)$  direction, the probability density out to a distance  $r_{\max}$  is

$$\frac{dP_i}{d\Omega}(r_{\max}, \ell, b) = \int_{r=0}^{r_{\max}} r^2 \rho_i(R, z) dr \quad (4)$$

which follows from the spherical volume element  $dV = r^2 dr d\Omega$  with solid angle  $d\Omega = \cos \ell d\ell db$  in Galactic coordinates. Inside the integral, the density depends on Galactocentric cylindrical coordinates given by

$$R(r, \ell, b) = \sqrt{R_\odot^2 + r^2 \cos^2 b - 2R_\odot r \cos \ell \cos b} \quad (5)$$

$$z(r, \ell, b) = r \sin b + z_\odot \quad (6)$$

We find the maximum distance  $r_{\max}$  in each direction by imposing a limiting apparent magnitude  $m_{\lim}$  (i.e., observed flux) for the supernova. The sightline distance follows from this limiting magnitude, together with the supernova absolute magnitude (i.e., luminosity) and the dust extinction, as explained in detail below in §3. Thus the probability of finding a SN of type  $i$  with a limiting magnitude  $m_V^{\lim}$  or brighter is

$$\frac{dP_i}{d\Omega}(m_V^{\lim}, \ell, b) = \frac{dP_i}{d\Omega} [r(m_V^{\lim}), \ell, b] \quad (7)$$

where  $r(m_V^{\lim})$  is solution to  $m_V(r) = m_V^{\lim}$ . And finally, the total probability of finding type  $i$  events is just

$$P_i(m_V^{\lim}) = \int \frac{dP_i}{d\Omega} d\Omega = \int \frac{dP_i}{d\Omega} \cos b db d\ell \quad (8)$$

Equations (4-8), are quite general—they hold for any axisymmetric distribution, and are straightforward to extend to non-axisymmetric cases. To evaluate them, we now build a model using the approximations noted above, turning first to the spatial distributions.

### 2.2 Models for Milky Way Stars, Dust, and Gas

Our fiducial model for the spatial distribution of supernova populations and dust in our Galaxy follows (Adams, et al. 2013), which uses the results of the TRILEGAL model (Girardi, et al. 2005) that uses stellar data to fit both a thin and thick disk, both in the double

**Table 1.** Properties of different types of supernovae

Property	Supernova Type	
Mechanism	Core-Collapse	Thermonuclear
Observed Type	II-P, II-L, Ib/c	Ia
Galactic Tracer	Thin Disk	Thick and Thin Disk
MW Rate <sup>a</sup> [events/century]	$3.2^{+7.3}_{-2.6}$	$1.4^{+1.4}_{-0.8}$

<sup>a</sup> From Adams, et al. (2013)

exponential form of eq. (3) above. The two components have scale parameters

$$(R_{\text{thin}}, h_{\text{thin}}) = (2.9 \text{ kpc}, 95 \text{ pc}) \quad (9)$$

$$(R_{\text{thick}}, h_{\text{thick}}) = (2.4 \text{ kpc}, 800 \text{ pc}) \quad (10)$$

In addition, TRILEGAL adopts a dust distribution

$$(R_{\text{dust}}, h_{\text{dust}}) = (2.9 \text{ kpc}, 110 \text{ pc}) \quad (11)$$

that is nearly identical to the thin disk, reflecting a common origin in cold, star-forming regions.

We follow the Adams, et al. (2013) associations of supernovae with these disk components, as summarized in Table 1. We model core-collapse SNe with the thin disk distribution above:  $\rho_{\text{CC}} = \rho_{\text{thin}}$ . We model Type Ia supernovae as having two components:  $\rho_{\text{Ia}} = (\rho_{\text{thick}} + \rho_{\text{thin}})/2$ : half arise in the thick disk, and half in the thin disk, corresponding to long and short delay times.

Two assumptions are worth highlighting. The TRILEGAL model, and thus ours, assumes an axisymmetric galaxy. This omits Milky Way features such as a bar and spiral arms. These may be important, as we will see below, and we plan to study their effects in future work. The last assumption we use is the time frame we are considering for supernovae is small enough to where the rate of supernovae occurring remains constant; this is certainly appropriate for historical supernovae.

Other ways to model the supernova distributions are possible. A full inventory of such approaches is beyond the scope of this paper, but here we highlight two. Green (2015) compiled a Galactic supernova remnant catalog (also discussed in §3.4 below), and used their longitude distribution to constrain the underlying supernova profile in Galactocentric radius. For an exponential form, the best-fit scale radius is  $R_{\text{SNR}} = 3.1 \text{ kpc}$ , based on a fit that omits the  $|\ell| < 10^\circ$  region where radio fore/backgrounds likely bias against remnant identification. The Green (2015) catalog includes both CCSN and SNIa, and so this represents a sort of average of the two; the TRILEGAL model we use has a very similar value for the thin disk (eq. 9) but a slightly smaller value for the thick disk (eq. 10). We thus expect our CCSN distribution to be similar to that of the SNR catalog regarding the longitude distribution, while our SNIa distribution reflects somewhat a more radially compact thick disk.

In order to compare our results with a dramatically different case, we consider the Galactic distribution of  $^{26}\text{Al}$  from Wang et al. (2020). This study presents an updated analysis of the sky distribution of the 1.809 MeV nuclear gamma-ray line from the radioactive decay of  $^{26}\text{Al}$ .  $^{26}\text{Al}$  production is likely dominated by massive stars, with SNIa production expected to be small. Thus the gamma-ray line emission should trace Galactic CCSN activity as averaged over the decay mean life  $\tau(^{26}\text{Al}) = 1.0 \text{ Myr}$ . Fitting the  $^{26}\text{Al}$  sky to a double exponential as in eq. (3), Wang et al. (2020) find scale parameters

$$(R_{^{26}\text{Al}}, h_{^{26}\text{Al}}) = (7.0^{+1.5}_{-1.0} \text{ kpc}, 800^{+300}_{-200} \text{ pc}) \quad (12)$$

Remarkably, the scale radius is more than twice that of our thin disk

value in eq. (9). Moreover, the scale height is eight times larger than our fiducial thin disk, and indeed is the same as our adopted thick disk value of eq. (10).

We will adopt the central values in eq. (12) to illustrate the effects of these large differences on our results.<sup>1</sup> In comparing this distribution to our fiducial model, it is well to bear in mind two caveats. First, if  $^{26}\text{Al}$  has significant nucleosynthesis sources other than massive stars, these will affect the resulting sky and spatial distributions. For example, asymptotic giant branch stars are likely  $^{26}\text{Al}$  producers (e.g., Doherty et al. 2014), and this longer-lived population could have a thicker height distribution. Second, Fujimoto, Krumholz, & Inutsuka (2020) have suggested that the  $^{26}\text{Al}$  sky map is substantially perturbed by foreground emission due to the Sun's embedding in a local source of  $^{26}\text{Al}$  nucleosynthesis. This intriguing result is consistent with other evidence of recent near-Earth supernovae, notably the detection of  $^{60}\text{Fe}$  as summarized in Fields et al. (2019). On the other hand, Krause et al. (2020) simulate the Galactic disk and find some  $^{26}\text{Al}$  is vertically dispersed as high as  $\sim 50 \text{ kpc}$  in the halo. With these caveats in mind, the  $^{26}\text{Al}$  distribution may represent a sort of upper limit to the possible lengthscales of the Galactic supernova distribution.

### 2.3 Integration Methods

We used two different methods to model the probability and visibility of supernovae across the sky, i.e., to solve eqs. (7) and (8). The first method, described in further detail in Appendix A, uses Newton's method to calculate how far along the sightline an observer can see before extinction causes the light to be too dim to see. The probability distribution of supernovae is then integrated along each sightline to produce  $dP/d\Omega$ . The 2D sky plots below are generated with this approach.

The second method, described in Appendix B, is a Monte-Carlo integration. We generate a large number ( $> 10^4$ ) of points representing supernovae, distributed according to the appropriate density function. The extinction and distance modulus of each point is then calculated and compared with the difference between the absolute magnitude of the SN type and the limiting visible magnitude. Their apparent magnitude is then compared across a range of limiting apparent magnitudes to compute  $P_i(m_V)$  and thereby generate Figure 12.

## 3 SUPERNOVA OBSERVABILITY: LUMINOSITIES, HISTORICAL EVENTS, AND RATES

The observability of a Galactic supernova depends on its intrinsic luminosity, its distance  $r$  from Earth, and on dust extinction along the line of sight. Specifically, a supernova with  $V$ -band absolute magnitude  $M_V$  and located at a distance  $r$  from Earth, will be observed with an apparent magnitude

$$m_V(r) = M_V + \mu(r) + A_V(r) \quad (13)$$

Here  $\mu(r) = 5 \log_{10}(r/10 \text{ pc})$  is the distance modulus, and  $A_V(r)$  is the extinction along the sightline. In this section we consider in turn  $M_V$  and its relation to the supernova light curve, and  $A_V$  and its relation to dust along the sightline.

<sup>1</sup> Wang et al. (2020) also fit to the sky distribution of the  $^{60}\text{Fe}$  gamma-ray decay lines, also finding a large scale radius and height. But the authors caution that these results are less reliable for this dimmer signal.

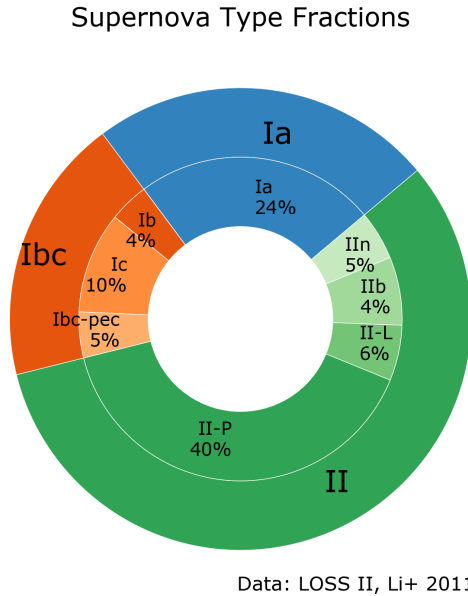


**Figure 1.** Intrinsic rates of supernovae: relative fractions of different types and sub-types as determined in a volume-limited sample in the nearby universe. From the Li et al. (2011) analysis of the LOSS survey data for 175 supernovae.

### 3.1 Naked-Eye Supernova Discovery

For historical supernovae, we are interested in the observability to the naked eye. We use the  $V$  passband as a proxy for the visible range. The naked eye has a sensitivity of at best  $V_{\text{lim}}^{\text{eye}} \simeq 6$  mag on a dark moonless night without light pollution (Clark 1990; Cinzano, Falchi, & Elvidge 2001).<sup>2</sup> We expect a supernova must appear substantially brighter than this in order to be discovered confidently and to be deemed worthy of historical note. Clark & Stephenson (1977) quote a minimum brightness for detection of  $m_V = 3$  in their Fig. 1.5. To our knowledge most magnitude estimates for historical supernova observations are brighter than this, though very difficult to estimate accurately (Stephenson & Green 2002).<sup>3</sup> In the context of the non-observation of Cas A, Shklovsky (1968) suggest that “this outburst would hardly have remained unnoticed if its visual magnitude had been brighter than”  $m_V = 4$ . van den Bergh & Dodd (1970) argue for a higher threshold of  $m_V = 2$ , based on a comparison between the modern observed bright nova rate versus the sparser Chinese records of guest stars.

For a fiducial threshold apparent brightness for historical events, we adopt<sup>4</sup> the most conservative (i.e., brightest) of these values,

$$m_{V,\text{lim}}^{\text{SN}} \simeq 2 \text{ mag}. \quad (14)$$

The detection threshold is clearly not sharply defined, so we will show how our results change for different values of  $m_{V,\text{lim}}^{\text{SN}}$ .

<sup>2</sup> In modern times, this corresponds to a class of 3 to 4 on the Bortle scale (Bortle 2001).

<sup>3</sup> For a modern comparison, SN 1987A was discovered visually at  $m_V \simeq 5$  mag, by several groups of professional astronomers who had been monitoring the Large Magellanic Cloud from a variety of observatories (Kunkel et al. 1987).

<sup>4</sup> Here we are grateful for private discussions with Ralph Neuhauser.

### 3.2 Supernova Luminosities

The peak luminosity corresponds to the peak absolute magnitude,  $M_V^{\text{peak}}$ ; while this sets an important scale, strictly speaking the explosion is only instantaneously this luminous. For a Galactic supernova to be identified and to enter the historical record requires repeated observations. This demands that the event is visible over an extended period of time so that observers would have confidence that a “new” or “guest” star is real. Difficulties with weather and observing season can lengthen the time needed for such observations. To attempt to capture this, we define  $M_V(\Delta t)$  to be the absolute magnitude at which the  $V$ -band-light curve has width  $\Delta t$ . In other words, over the timescale  $\Delta t$  the supernova is at least this luminous:  $M_V \leq M_V(\Delta t)$ . We thus call this a *sustained luminosity* for interval  $\Delta t$ . For a singly-peaked supernova light curve, the shorter  $\Delta t$ , the closer the sustained magnitude is to the peak absolute magnitude. The *minimum* duration  $\Delta t$  required for historical supernova detection is of course uncertain, and so we determine sustained luminosities for a range of durations.

Table 2 shows sustained luminosity values for major supernova varieties. These results drew from the data compilation and visualization in the the Open Supernova Catalog<sup>5</sup> (Guillochon et al. 2017). For each supernova type or subtype, we chose a “template” or exemplar event that: (a) showed consensus in the type or subtype classification, (b) had among the largest apparent brightness, (c) was well observed in the  $V$  band for at least 180 days, and (d) was seen within the last 20 years. For each event, we found  $M_V^{\text{peak}}$  and  $M_V(\Delta t = 30, 60, \& 90 \text{ days})$ . As noted in Li et al. (2011), intrinsic variations within the different subtypes are typically  $\sigma(M) \sim 1$  mag. Also, we have not attempted to correct for extinction in the host galaxy; these events were generally in the outskirts of face-on galaxies and where estimates exist, they are less than 1 mag.

In Table 2 we see that the sustained luminosities can be much smaller than the peak values. For example,  $M_V(90 \text{ days})$  can be 2 magnitudes dimmer than the peak values. Turning to specific types, SNIa have the highest peak luminosity, but at  $\Delta t \geq 60$  days, the core-collapse events have higher sustained luminosity. This reflects difference in the light curve shapes over these timescales.

For the core-collapse events, we see the the most common subtype, II-P (“plateau”), have the highest sustained luminosity  $\geq 60$  days, due to the extended plateau of brightness that gives them their names. We also see that the spread among the core-collapse subtypes grows from 0.8 mag at peak to 3.7 mag at 180 days. In the results below we adopt the Table 2 value for SNIa, while for CCSN, we take a weighted average of each according to the relative abundances shown in Figure 1.

Stephenson & Green (2002) show that the 5 confirmed historic events were visible for timescales ranging from 6 months (SN 1181) to 3 years for SN 1006. Thus a choice of 90 days visibility would be shorter than all known historical supernovae, though presumably enough time to allow for detection. We will adopt  $M_V(90 \text{ days})$  for which we have the best data, but will compare with results assuming  $M_V(180 \text{ days})$ .

We assume all core-collapse subtypes follow the same thin-disk spatial distribution. This implies that the different subtypes occur with the same relative frequencies throughout the Galaxy. If this were not the case, it could affect our results if the intrinsically brighter events were concentrated differently than the rest. In fact, Kelly,

<sup>5</sup> <https://sne.space/>

**Table 2.** Supernova  $V$ -band absolute magnitudes: peak and sustained luminosities

SN Type	Template	Peak $M_V^{\text{peak}}$	Sustained $M_V$ ( $\Delta t$ )				References
			$\Delta t = 30$ days	60 days	90 days	180 days	
Ia	2011fe	-17.7	-16.9	-15.3	-14.7	-12.8	Munari et al. (2013); Brown et al. (2014); Stahl et al. (2019)
II-P	2012aw	-17.0	-16.8	-16.7	-16.5	-13.9*	Munari et al. (2013); Brown et al. (2014); Dall’Ora et al. (2014)
II-L	2014G	-17.1	-16.3	-15.6	-14.2	-11.8*	de Jaeger et al. (2019)
Iib	2011dh	-16.8	-16.5	-16.0	-15.3	-12.3*	Sahu, Anupama, & Chakradhari (2013); Bartunov, Tsvetkov, & Pavlyuk (2007)
IIn	2011ht	-16.8	-16.5	-16.1	-15.6	-10.2*	Mauerhan et al. (2013); Bartunov, Tsvetkov, & Pavlyuk (2007); Brown et al. (2014)
Ib	2016coi	-17.5	-16.0	-15.3	-14.9	-13.4	Prentice et al. (2018); Brown et al. (2014)
Ic	2007gr	-16.7	-15.3	-14.5	-14.0	-12.3	Bartunov, Tsvetkov, & Pavlyuk (2007); Bianco et al. (2014)

\*Estimated

Kirshner, & Pahre (2008) studied location of 504 low-redshift supernovae in their host galaxies. They found that Type Ia, Ib, and II events trace the galaxy light, while Type Ic events are preferentially located in the brightest regions of their hosts. Later work shows that Type Iib and broad-line Type Ic and events favor the bluest regions with indications of lower metallicity (Kelly & Kirshner 2012). Our work does not capture these complex effects.

### 3.3 Dust Extinction

We calculate the extinction in our Galaxy in a heliocentric coordinate system. The optical depth in the  $V$  passband is the integral over a line of sight:

$$\tau_V = \kappa_V \int_{\text{los}} \rho ds = \kappa_V \Sigma = \frac{2 \ln 10}{5} A_V \quad (15)$$

with  $\Sigma = \int_{\text{los}} \rho ds$  the mass column along the sightline, and  $\kappa_V$  the opacity. This integral in general is not simple since the density along each individual line of sight varies throughout the sky, and thus we must evaluate it numerically.

We normalize to the extinction sight line of Galactic center, which we take to be  $A_{V,GC} = 30$  following Adams, et al. (2013). This gives

$$A_V(r_{\text{max}}, \ell, b) = \frac{\int_0^{r_{\text{max}}} \rho_{\text{dust}}(R, z) dr}{\Sigma_{GC}} A_{V,GC} \quad (16)$$

where  $r_{\text{max}}$  is the same as in eq. (4). The denominator in eq. (16) is the mass column  $\Sigma_{GC}$  to the Galactic Center; for our case of axisymmetry with an exponential radial drop-off, this is  $\Sigma_{GC} = \rho_{\text{dust},0} R_i (1 - e^{-R_{\odot}/R_i})$ . Equations (5) and (6) give the conversions from heliocentric sightline coordinates to the Galactocentric coordinates that appear in the dust distribution.

Our simple double-exponential model for the Galactic dust distribution is only a rough approximation. Adams, et al. (2013) showed the effect of using more sophisticated dust distributions based on observed extinction maps. They found that the qualitative results for Galactic supernova visibility were similar, and that generally results for this simple model fell between those based on those of Schlegel, Finkbeiner, & Davis (1998) and a modified version with lower  $E(B - V)$  reddening similar to that in updated later work Schlafly et al. (2010); Schlafly & Finkbeiner (2011). Subsequently, Green et al. (2014) and Green et al. (2019) presented full 3D dust maps based on PAN-STARRS and 2MASS data<sup>6</sup>. These very useful tools have some limitations for our purposes, with accuracy limited to distances  $< 10$  kpc for the low Galactic latitudes of most interest

<sup>6</sup> <http://argonaut.skymaps.info/>

to us. Nevertheless, it would be of great interest to incorporate these maps in future studies.

### 3.4 Data: Supernova Remnants and Historical Supernovae

We will calculate both the intrinsic (all brightness) sky distributions of supernovae, as well as the expected sky map of naked-eye events. We will compare these predictions with observed events. To represent the full complement of known Galactic supernovae, we use the Green (2019) catalog of 294 Milky-Way supernova remnants. Most of these objects do not have secure distances or type designations. The catalog is based largely on radio detections, so should not suffer from extinction effects, due to the Milky Way transparency in the radio. However, as Green (2015) elucidates in detail, the available radio surveys are highly nonuniform for several reasons. They have a lower sensitivity to SN remnants in inner Galaxy, due to the high radio background in these regions. Moreover, northern radio surveys have been more numerous and deeper than their southern counterparts. Also, additional biases could arise if supernova remnant lifetime and brightness varies with location in the Galaxy, as is likely.

Turning to historic supernovae, we draw upon the extensive studies in the Clark & Stephenson (1977) and Stephenson & Green (2002) monographs, and subsequent update Green & Stephenson (2017). There are 5 confident historic supernovae on record, occurring in the years 1006, 1054, 1181, 1572, and 1604. SN 1006, the oldest supernova on record, is also the southernmost and was likely the brightest as well ( $m_V^{\text{peak}} \approx -7$ ). At its peak, it was easily seen during the day and was tracked by astronomers for 3 years. SN 1054, whose remnant is commonly known as the Crab Nebula, is the second oldest and most studied, being extensively cataloged by Chinese and Japanese astronomers. Other than SN1006, it is the only SN that was recorded as being seen during the day, and was visible for 21 months, with an estimate peak brightness  $m_V^{\text{peak}} \approx -3.5$ . Remarkably, SN 1054 is located at almost the anticenter of the Milky Way, which will be important in our results below. SN1181 was seen by Chinese, Japanese, and Arab astronomers for 6 months, its peak brightness is estimated at  $m_V^{\text{peak}} \approx 0$  or perhaps slightly higher Stephenson & Green (2002). SN 1572, also known as Tycho’s supernova, was seen for 18 months and attained a peak brightness of about  $m_V^{\text{peak}} \approx -4$  (Stephenson & Green 2002). The last supernova seen in the Milky Way was SN1604, which was seen by Chinese, Korean, and European astronomers, including most famously Johannes Kepler. Clark & Stephenson (1977) infer a rough light curve that spanned 12 months, and find a peak magnitude around  $m_V^{\text{peak}} \approx -3$ .

For these confirmed supernovae, the basic types are confidently

established for four the five. Both SN 1054 and 1181 were core-collapse events, as confirmed by the observation of a pulsar in each remnant. The Crab is thought to be II-P (Smith 2013), which would be a signature of interactions with a circumstellar medium. SN 1181 seems to be underluminous and with circumstellar material, but even so the type is unclear: (Kotthes 2013) proposes Ib, Ic, II-L, or underluminous II-P. SNe 1006, 1572, and 1604 are identified as Type Ia events. For SN 1006 this is primarily because of its location outside of the Galactic plane, lack of nearby OB association, and high luminosity and lack of compact object in the remnant (Katsuda 2017, and refs. therein). In the case of Tycho this has been confirmed by light echo spectroscopy (Krause et al. 2008). For Kepler this based on their remnant composition and lack of a compact object in the remnant (Vink 2017, and refs. therein).

It is worth noting that all five confirmed historical supernovae are visible from Earth’s northern hemisphere, as seen below in Fig. 11. 7. We suspect this is a selection effect, reflecting that fact that most searches to date focused on civilizations in the northern hemisphere, searching Chinese, Japanese, Korean, Indian, Arabic, and European records. We expect that interesting results await searches in records from the global South.

Indeed, the Galactic Center is best observed from the south. This may play a role in the curious paucity of known historical events there, which we will see contrasts with our model predictions that this should be the region of maximum probability.

Several additional events or remnants have been proposed as historical SNe, but are not (yet) supported by the same weight of evidence of the five ‘confirmed’ events. We will highlight the three of these that Green & Stephenson (2017) consider likely, and that are associated with specific remnants: Cas A, SN 185 and SN 386. The Cas A remnant has an associated pulsar and thus it was a CCSN. As noted above, although there is some debate, it seems unlikely Flamsteed saw this event and thus we do not count it among confident/confirmed historical SNe.

Chinese records describe a guest star in AD 185, whose position is most likely associated with the G315.4-2.3 (RCW 86) remnant whose age is consistent (Vink et al. 2006). The remnant location is consistent with an OB association, and thus suggests an origin in a core-collapse explosion (Vink, Kaastra, & Bleeker 1997). Similarly, one Chinese source records a guest star in AD 386, which has been associated with the G11.2-0.3 remnant that contains a pulsar and thus was a CCSN.

### 3.5 Supernova Rates and Frequencies

A number of methods have been used to estimate the present rates of supernovae in the Milky Way. Adams, et al. (2013) use historic supernovae and their calculations of naked-eye observability to infer global rates for the two main supernova types. These appear in Table 1, where we see that core-collapse events occur at about double the rate of Type Ia explosions. Furthermore their total Galactic rate of both types is  $\mathcal{R}_{CC} + \mathcal{R}_{Ia} = 4.6^{+7.4}_{-2.7}$  events/century, so that the  $1\sigma$  range spans a mean interval of  $\sim 8$  to 50 years per event. Thus we can reasonably hope for a event somewhere in the Galaxy within a human lifespan.

Recently, Rozwadowska, Vissani, & Cappellaro (2021) survey this and other methods of estimating Galactic CCSN rates, and in a

combined analysis they find  $\mathcal{R}_{CC} = 1.63 \pm 0.46$  events/century. This is consistent within errors with the Adams, et al. (2013) result, but reports a central value that is almost a factor of 2 smaller, and a significantly smaller error.

Core-collapse events display a range of observational behaviors that have been grouped into subtypes. The intrinsic frequencies for these subtypes are summarized in in Fig 1, which presents the data from the Li et al. (2011) volume-limited analysis of the LOSS-II survey. We see that Type II-P supernovae are the most common core-collapse events.

## 4 RESULTS: MILKY WAY SUPERNOVAE IN AXISYMMETRIC GALACTIC MODELS

We now present our predictions for the intrinsic and observed supernova distributions for our axisymmetric model of the Milky Way supernova distribution.

### 4.1 The Intrinsic Galactic Supernova Sky Distribution

We begin with the intrinsic sky distributions for both core-collapse and Type Ia supernovae. That is, the probability per unit area on the sky that there will be a supernova of this type, regardless of its observability. To do this we use eq. (4) to calculate  $dP/d\Omega(r_{\max}, \ell, b)$  for each supernova type, setting the line of sight distance  $r_{\max}$  to reach the edge of the Galaxy, which we take to be at  $R_{\max} = 6R_{\odot}$ ; our results are insensitive to this cutoff choice.

Our results appear in Figs. 2 and 3, which show the supernova probability distribution in the regions of the sky where it is non-negligible, namely near the Galactic plane. To increase legibility, these and all sky plots we show are zoomed and *stretched* in latitude, i.e., the vertical angular scale is not equal to the horizontal scale.<sup>8</sup> For both supernova types, we see that the region of highest probability is in the central quadrants of the Galaxy and close to the Galactic midplane.

Core collapse events are confined to within a few degrees of the plane, due to their origin in the thin disk. The characteristic angular half-width  $h_{\text{thin}}/R_{\odot} \sim 0.6^{\circ}$  compares well with the thickness of the peak region of Fig. 2. On the other hand, SNIa in our model have a component in the thick disk that has  $h_{\text{thick}}/R_{\odot} \sim 5^{\circ}$ , which explains the significantly higher vertical extension in Fig. 3.

For both core-collapse and Type Ia events, there is a subtle shift: the probability density peak lies not at the Galactic center itself, but is slightly shifted to negative latitudes. This offset to the Galactic south arises due to the height  $z_{\odot} = 20$  pc of the Sun in the Galactic plane. so that the sightline to the center is inclined by an angle  $\simeq z_{\odot}/R_{\odot} \simeq 0.13^{\circ}$  with respect to the geometric Galactic plane. Our vantage point slightly above the midplane means that the source density is slightly higher for sightlines at negative Galactic latitude than at the same corresponding positive latitude. We have run models varying the solar height to show that this is the source of the asymmetry, and to verify that the distribution is symmetric and peaks that the Galactic center when we set  $z_{\odot} = 0$ .

Our model thus predicts that the next Galactic SN is most likely to occur at low Galactic latitudes near the Galactic center, as one would guess. Specifically, the CCSN distribution shows the highest probability for  $|b| \lesssim 1^{\circ}$  and  $|l| \lesssim 45^{\circ}$ . The heart of the Type Ia distribution is slightly broader in both dimensions, with  $|b| \lesssim 2^{\circ}$  and  $|l| \lesssim 60^{\circ}$ .

<sup>7</sup> All but the Crab are located in the northern Galactic hemisphere, as also seen in Fig. 11. Presumably this arises because of the partial overlap between the Galactic and equatorial north.

<sup>8</sup> An earlier version of these plots appears in Strader, et al. (2018).

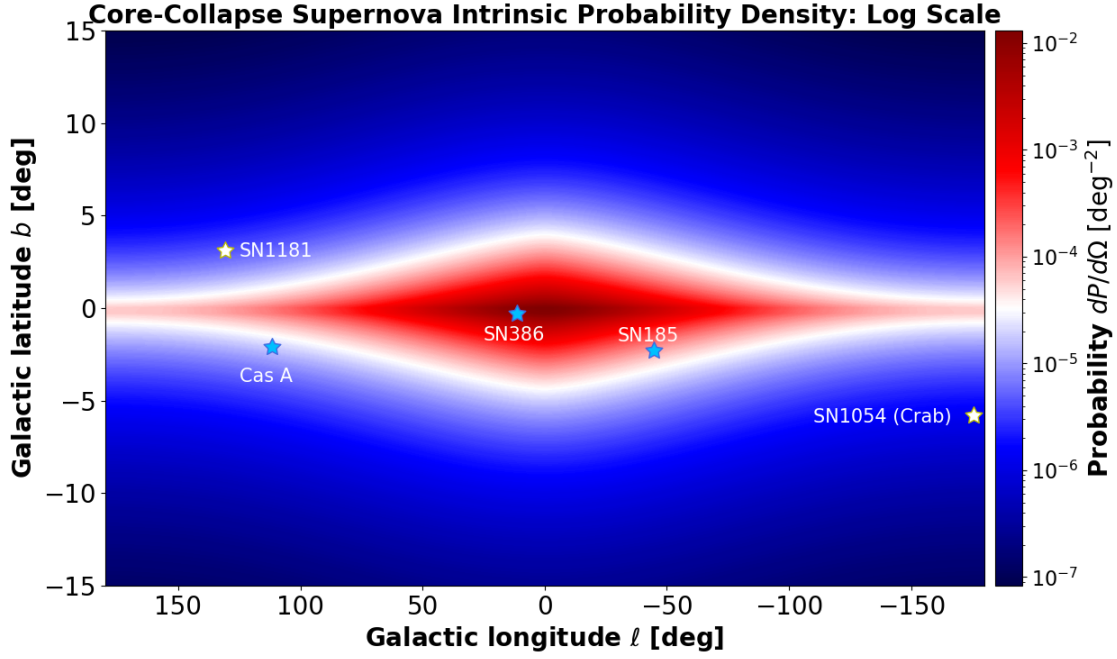


**Figure 2.** Sky plot of the probability density for all Milky Way core-collapse supernovae, in units of probability per square degree; *note the logarithmic scale*. Shown in Galactic coordinates is a zoom into the region around the Galactic plane spanning all longitudes but only latitudes  $|b| \leq 15^\circ$ . Note that the vertical dimension is stretched compared to the horizontal in order to highlight the interesting regions. The intrinsic probability density is shown, that is, the map plots the likelihood for sky positions for all CCSN to occur, regardless of distance, apparent magnitude or extinction effects.

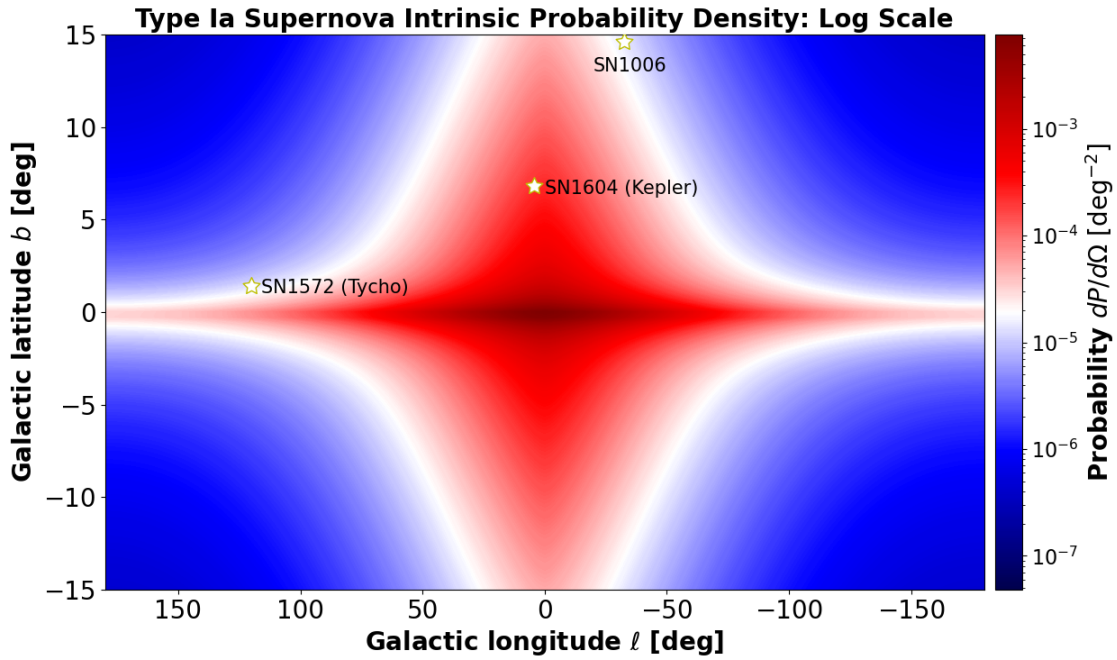


**Figure 3.** Similar sky plot to 2, but for the intrinsic distribution of Type Ia supernovae. *Note the logarithmic scale*.

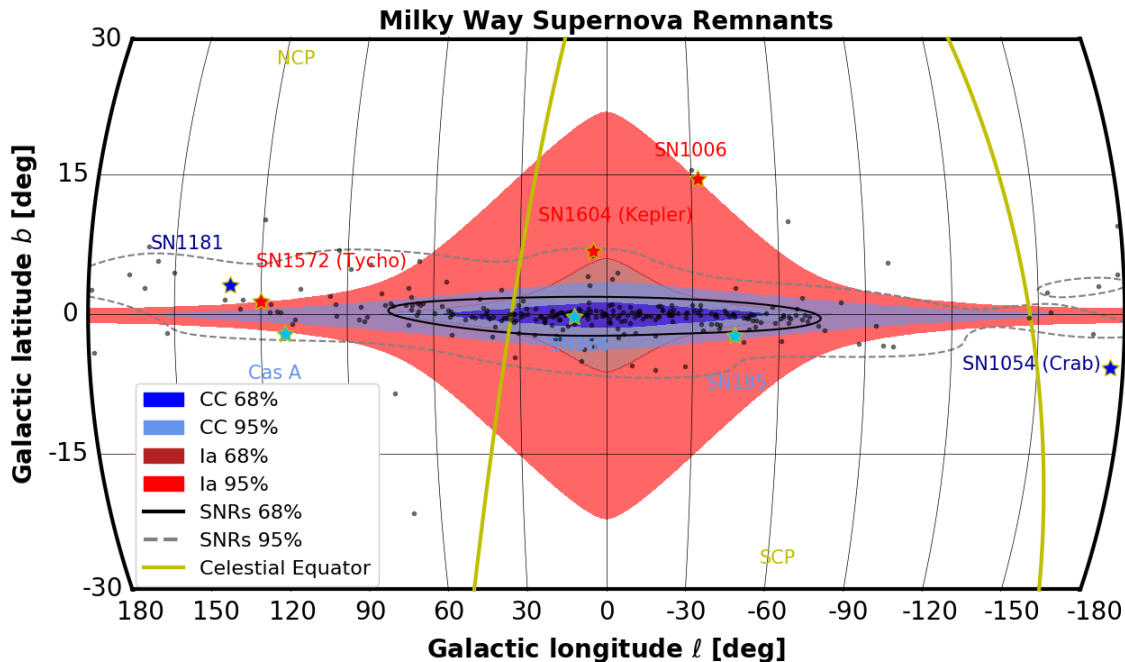


**Figure 4.** Zoom-out map of supernova probability showing ‘zoom-out’ views of the distributions of CCSN as in Fig. 9 and Type Ia events as in Fig. 10. In Galactic coordinates and Mollweide projection. Contours are drawn for  $dP/d\Omega|_{\text{contour}} = (0.3, 1, 3)\text{sr}^{-1}$ , for CCSN (blue) as in Fig. 2, and SNIa (red) as in Fig. 3. Points show the 294 SN remnants from the Green (2019) catalog; the dark contour lines reflect a kernel density estimate and enclose 68% and 95% of the events. Historical supernovae are labeled: confirmed SNIa events are shown in red; confirmed CCSNe are shown in dark blue, while possible CCSNe are shown in light blue. We see that confirmed historical events appear to be outliers in the remnant distribution. Celestial equator and poles are shown; we see that the asymmetry in positive and negative latitudes suggesting incompleteness in the third Galactic quadrant.

Figure 4 plots both CCSN and SNIa predictions in an zoom-out view. We also plot the known Milky Way supernova remnants from the Green (2019) catalog. Because these mostly do not have well-established types, we do not attempt to distinguish CCSN vs SNIa remnants except for historical events. We see that the remnant distribution broadly follows the predictions, with most supernovae found in the central quadrants and at low latitudes. We have used a kernel density estimate to derive a probability density of the remnants; the solid black (dashed gray) contour in Fig. 4 encloses 68% (95%) of the observed remnants.

Comparing the observed remnants and the model prediction reveals areas of both agreement and disagreement. We see that the theory contours enclosing 68% of the total probability (darker shades of blue and red) are in rather good agreement with the remnant 68% region (solid black line). All three have a similar longitude extent. In latitude, the observed remnant width is larger than the model CCSN and smaller than the model SNIa, as we would expect given that the remnants sum both. On the other hand, we note that the 95% contours for the models (lighter blue and red shades) and the data (dashed gray line) are not particularly well-matched. In particular, the SNIa model predicts more high latitude events than are seen in remnants. And the observed remnants in the outer quadrants have a thicker width than either model.

The sky distribution of remnants has some notable features suggestive of incompleteness. We see that there are more high-latitude events in the outer quadrants (i.e.,  $|\ell| > 90^\circ$ ) than in inner quadrants. As Green (2015) notes, this likely reflects the lower sensitivity in the Galactic center due to the higher background of diffuse radio emis-

sion in that region. There is also a notable asymmetry in the counts at the outer quadrants, with higher counts in the second quadrant than the third. This too was noted by Green (2015), who points out that the second quadrant is in Earth’s northern hemisphere and thus has enjoyed more and deeper study at radio wavelengths. In summary, Fig. 4 suggests there remain supernova remnants to be found at higher latitudes in the inner quadrants, and in the southerly third quadrant.

The placement of historical supernovae in Fig. 4 is revealing. The map reveals the confirmed historical supernovae, marked as stars and labelled, seem to be for the most part outliers in the SN remnant distribution. All five confident events lie outside the 68% contour of the remnant population, and both SN 1006 and SN 1054 lie outside the 95% contour. All historical supernovae are found high latitudes compared to the rest of the distribution. The two confirmed core-collapse supernovae SN 1054 and SN 1181 both lie in the two outer Galactic quadrants; SN 1054 is also at a high latitude and nearly at the Galactic anticenter. Of the three confirmed historical Type Ia SNe, SN 1572 is in an outer quadrant. SN 1006 is in an inner quadrant but has the third highest  $|b|$  of the 294 object sampled! Indeed, of all confident historical supernovae only SN 1604 is in a region at low latitude near the Galactic center.

Of course, it is to be expected that historical supernovae do not follow the full distribution of Galactic supernovae because naked-eye observations and historical records only capture the brightest events. To properly compare the historical SN events with expectations, we must account for their observability, to which we now turn.



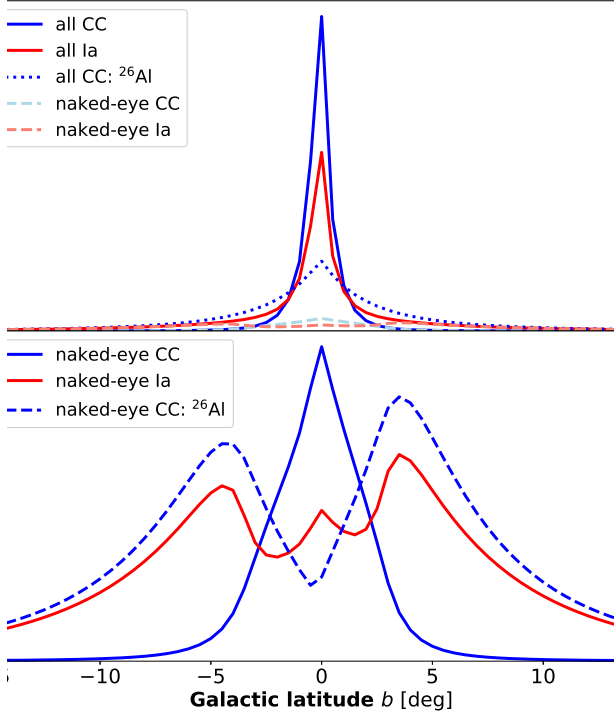


**Figure 5.** Distribution of Milky Way supernovae in Galactic latitude. *Top:* intrinsic and naked-eye distributions on the same scale. *Bottom:* zoom into naked-eye distribution.

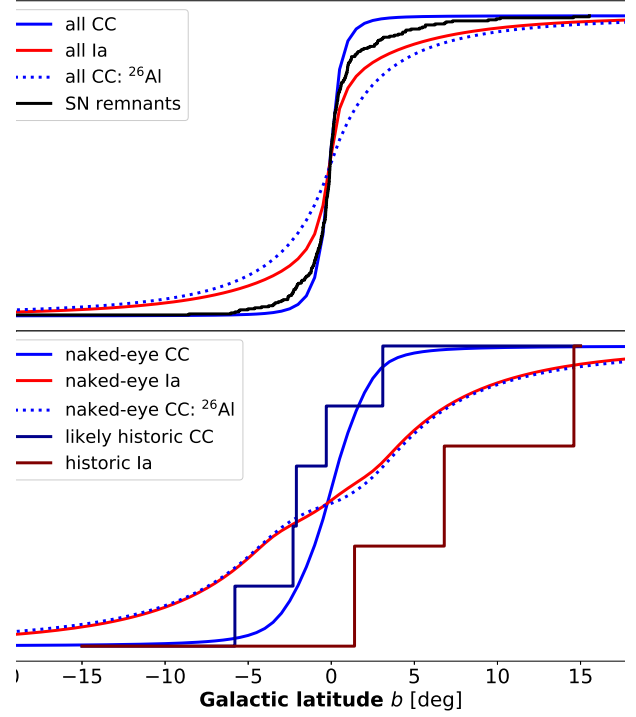


**Figure 7.** Cumulative distribution of supernova latitudes. *Top:* intrinsic distributions compared to the Green (2019) catalog of observed SNRs. *Bottom:* naked-eye distributions compare to historic supernovae.

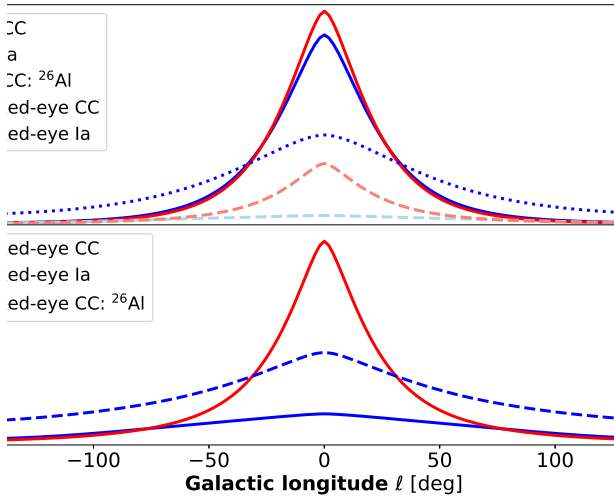


**Figure 6.** As in Fig. 5, but for supernova longitudes.

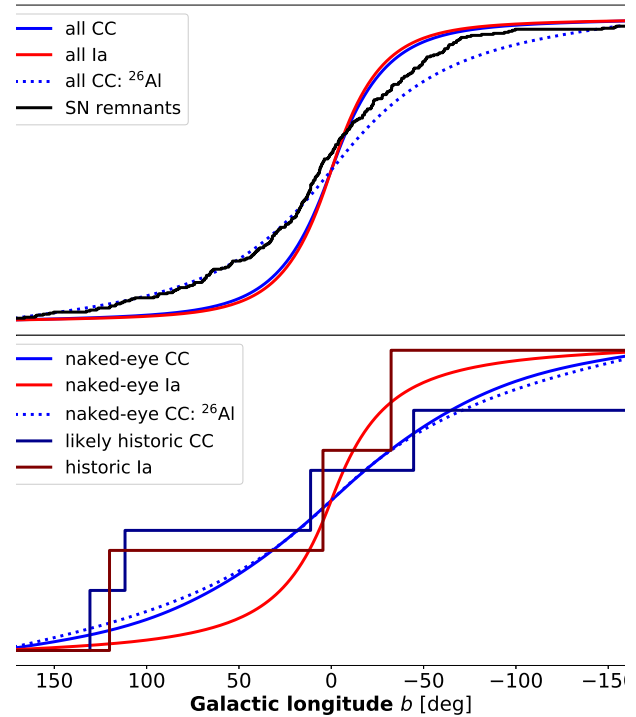


**Figure 8.** As in Fig. 7 but for the cumulative distributions in longitude.

## 4.2 The Distribution of Naked-Eye Events and Comparison With Historical Supernovae

After taking into account the dust and its visible band extinction, we arrive at the sky plots in Figures 9 and 10. These plots describe the probability density of a visible SN occurring in the sky. The black contours enclose 68% of the total probability, while the gray contours enclose 95%. The addition of dust extinction shows that the Galactic center is no longer the highest probability, due to the large optical depths to the Galactic center and beyond. Two regions slightly above and below the center of the Galaxy become the highest probability of observing a SN for both core-collapse and Type Ia explosions.

Furthermore, for both core-collapse and Type Ia events, the peak in the region slightly north of the Galactic center is higher than its counterpart south of the center. This asymmetry arises from the Sun’s non-zero height above the Galactic plane. As noted in the previous section, the source density is higher for sightlines at negative latitudes. But the dust density is also slightly higher for the same sightlines, and the effect of extinction dominates.

We have adopted a minimum apparent magnitude  $m_V^{\text{lim}} = 2$  for Figs. 9 and 10 and supernova magnitudes corresponding to the  $\Delta t = 90$  day sustained luminosity of  $(M_V^{\text{CC}}, M_V^{\text{Ia}}) = (-15, -14.7)$ . Since these luminosities are very similar, the differences between the plots almost entirely reflect the difference in the underlying geometry, i.e., that the SN Ia distribution has a thick-disk component. We have explored the effect of choosing any one of these magnitudes to be brighter or dimmer by  $\pm 2$  mag. The changes are not dramatic, but as expected, the distributions become somewhat broader in their extension in both latitude and longitude when made dimmer.

Figures 9 and 10 also show the locations of the well-established historical supernovae. Despite only having a few events, the comparison is striking, as foreshadowed in Fig 4. Core-collapse events appear in Fig. 9, where we see that the two confirmed historical discoveries, SN 1054 and SN 1181, both lie in regions of low probability. SN 1181 is at the edge of the 95% contour, and SN 1054 is well outside of it. Both events are strongly offset in both latitude and longitude from the predicted favored regions near the Galactic center. Indeed, the two supernovae both lie in the outer (2nd and 3rd) Galactic quadrants, with the Crab almost exactly at the anticenter!

Figure 9 also shows three potential historical CCSN events. Cas A has a location very similar to SN 1181, lying in the 2nd quadrant and at a latitude above the range our model favors, somewhat outside the 68% contour but well within the 95% region. By contrast, if SN 386 is indeed associated with the G11.2-0.3 remnant and pulsar, it lies very close to the Galactic center and is in the highest probability region of all of the events shown. Finally, SN 185 is less central but still in the 4th quadrant and in a region of substantial probability—both this event and SN 386 lie inside the 68% contour. Thus, if these two candidate events could be confirmed, they will partially relieve the mismatch between the observed events and our model predictions.

Turning to Type Ia events in Figure 10, we find the situation is somewhat improved. Once again, the historical discoveries avoid the regions of highest probability around (but not precisely at) the Galactic center. But SN 1604 and 1572 (Kepler and Tycho, respectively) both lie much closer to the high probability regions than the CCSN. Kepler lies at very central longitudes but is at a high latitude compared to our peak region; it is inside the 68% contour. Tycho is complementary in that it lies at low latitudes but at larger longitudes than our peak region—indeed, it is in the second Galactic quadrant. Finally, SN 1006 is at moderate longitude compared to our predictions, but lies at  $b \sim 15$ , a very high latitude relative to our high-probability regions. Indeed, SN 1006 has the 3rd highest  $|b|$  of all of the super-

nova remnants in the Green (2015) catalog. Nonetheless, both SN 1006 and SN 1572 lie inside the 95% region.

Thus we see that except for SN 1604, the confident historical supernovae of both types have sky locations outside of the regions our model favors. Our calculations include the effects of dust extinction, so the discrepancies must reflect one or more assumptions we have made. Possible reasons for these mismatches are discussed below in §5.

Fig. 11 presents a zoom-out summary of our predictions and the historical data for both supernova types. Models shown are our fiducial model with  $m_{\text{vis}} = 2$  mag, as in Figs. 9 and 10. The darker (lighter) blue and red regions enclose 68% (95%) of the total probability of seeing CCSN and SNIa respectively, as in as in Figs. 9 and 10. The distributions are thus broader than those in the intrinsic distribution seen in Fig. 4 because the visible supernovae are closer.

Fig. 11 also shows the celestial equator and celestial poles. As noted in §3.4 and in Adams, et al. (2013), the best-studied historical supernova records are from civilizations in the northern hemisphere. These records thus are less sensitive to events in the southern sky, and completely insensitive to supernovae in the far south. We note that SN 1006 at  $\delta = -40^\circ$  is even further south than the Galactic center, yet was seen in the north, but it was also the brightest SN known.

It is therefore possible that there were additional historical SNe that were seen by only southern observers. These events may have been recorded in some way. For example, the southernmost part of the Galactic plane is at  $\ell = 302.9^\circ = -57.1^\circ$ .<sup>9</sup> This lies in the inner region of the plane—the 4th quadrant—and has significant probability in both our CC and Ia models.

Furthermore, southern observers would have had excellent views of SN 1006, and better views of SN 1064; both would have been much higher above the horizon than for northern observers and thus visible for longer, from more locations, and with less air-mass. Furthermore, the proposed SN 185 and 386 locations lie in the southern sky, and would be of particular interest to find in historical records. On the other hand, by unfortunate coincidence, SN 1181 and 1572 are both at longitudes close to  $\ell = 123^\circ$ , where the Galactic plane has its maximum northern excursion, and both lie at  $\delta \approx +65^\circ$ , making them two of the northernmost known supernova remnants. Thus, these events would have been difficult or impossible to be seen from all but the lowest southern latitudes.

We thus encourage efforts to recover and study historical astronomical records from southern hemisphere. These could provide new insights into known or suspected historical supernovae. Indeed, the known events can also serve as “calibration” points in interpreting ancient records. And it is possible that completely new events await (re)discovery in southern archives.

## 4.3 Marginalized Results: Latitude and Longitude Distributions

We can marginalize our 2-D all-sky distributions to obtain 1-D distributions of supernovae vs latitude or longitude. The latitude distribution is given by

$$\frac{dP}{db} = \int \frac{dP}{d\Omega} \frac{d\Omega}{db} = \frac{1}{\cos b} \int \frac{dP}{d\Omega} d\ell. \quad (17)$$

<sup>9</sup> The maximum excursion of the Galactic plane from the celestial equator has a declination  $|\delta| = 90^\circ - b_{\text{NCP}} = 62.9^\circ$  at longitudes  $\ell = (\ell_{\text{NCP}}, \ell_{\text{SCP}}) = (122.9^\circ, 302.9^\circ)$ , where  $(\ell_{\text{NCP}}, b_{\text{NCP}})$  is the north celestial pole location in Galactic coordinates.

**Table 3.** Central Intervals for Marginalized Distributions in Fiducial Models

Model	latitude $ b $ [deg]		longitude $ \ell $ [deg]	
	68%CL	95%CL	68%CL	95%CL
Intrinsic CCSN	0.7	2.4	29	88
Intrinsic SNIa	2.5	14	27	79
Intrinsic CCSN: <sup>26</sup> Al	4	17	64	152
Naked-Eye CCSN	2	6	29	88
Naked-Eye SNIa	8	24	35	118
Naked-Eye CCSNe: <sup>26</sup> Al	9	29	87	164

This appears in Fig. 5 that shows both intrinsic and naked-eye cases in our fiducial model and for the for the <sup>26</sup>Al-based CCSN distribution. As expected, we see that for both intrinsic and naked-eye cases, the fiducial CCSN distribution is the narrowest, followed by the SNIa then <sup>26</sup>Al models. This reflects the differences in scale heights. We note that the SNIa distribution averages thin and thick disk components corresponding to the fiducial and <sup>26</sup>Al-based CCSN models. Thus the SNIa latitude distribution is intermediate. Also as expected, we see that the naked-eye events have a wider latitude distribution than their corresponding intrinsic cases. This reflects the shorter distances to the naked-eye events, leading to the scale height subtending a larger angle.

The longitude distribution is given by

$$\frac{dP}{d\ell} = \int \frac{dP}{d\Omega} \frac{d\Omega}{d\ell} = \int \frac{dP}{d\Omega} \cos b \, db \quad (18)$$

and appears in Fig. 6. Here the scale radius is the controlling factor. Thus, the intrinsic CCSN and SNIa distributions are very similar, reflecting the similar scale radii, while the intrinsic <sup>26</sup>Al distribution is broader. For the case of the naked-eye events, the extinction towards the Galactic center down-weights this region strongly for the CCSN, leading to a broader longitude distribution. This effect is much less pronounced for the other cases where the scale height is larger.

Finally, we can integrate the 1-D results to obtain cumulative distributions in both latitude and longitude:

$$P(< b) = \int_{-\pi/2}^b \frac{dP}{db} \cos b \, db \quad (19)$$

$$P(> \ell) = \int_{\ell}^{\pi} \frac{dP}{d\ell} \, d\ell \quad (20)$$

These are of particular interest because these allow direct comparison with the cumulative distributions of observed SNe. These also give all-sky total probabilities of observable supernovae to be  $P_{CC,tot} = 14\%$  and  $P_{Ia,tot} = 33\%$ .

Fig. 7 shows our predicted cumulative latitude distributions, and Table 3 quantifies the angular scales at which 68% and 95% of events are contained. The top panel gives the results for our intrinsic models shown in the upper panel of Fig. 5. To represent observations, we show the cumulative distribution of the Green (2019) SNR catalog that combines CCSN and SNIa; this is somewhat wider on the  $|b| > 0$  side, perhaps reflecting the bias towards more extensive observations from the terrestrial northern hemisphere. We see that the observed SNR data lies between the predictions of fiducial CCSN and SNIa models, which is as expected given that the data includes remnants from both SN types. On the other hand, the very broad distribution based on <sup>26</sup>Al observations is in strikingly poor agreement with the observer SNR population. This suggests that either <sup>26</sup>Al has important sources other than SNe, or it could be due to the Sun's embedding in local <sup>26</sup>Al source (Fujimoto, Krumholz, & Inutsuka 2020; Krause et al. 2020); see discussion in §5.

In the lower panel of Fig. 7 we show the cumulative distribution of naked-eye supernovae, corresponding to the lower panel of Fig. 5. We see that the narrow fiducial CCSN distribution gives sharp rise around  $\ell = 0$ , while the wider SNIa and <sup>26</sup>Al-based distributions show a much more gradual rise. We also show the cumulative distributions for confident and likely historic supernovae of each type. We see that the historic CCSN events extend to larger  $|b|$  than predicted in the model, particularly the first step that corresponds to SN 1054. Turning to SNIa, it is striking that all three events are in the Galactic north, which leads to a strong mismatch with the predictions that are by construction north-south symmetric. This aside, it is again clear from the plot and from Table 3 that our model does not assign high probability to high-latitude events. Finally we note that the <sup>26</sup>Al-based distribution is very similar to that of SNIa, reflecting the same large scale height value used in both.

The corresponding cumulative longitude distributions appear in Fig. 8 for the same models and observed populations as in Fig. 7. In the top panel we show the intrinsic models. We see that the fiducial CCSN and SNIa cumulative longitude distributions are very similar, reflecting the similar scale radii, while the <sup>26</sup>Al-based distribution is substantially broader. Interestingly, the Green (2019) SNR distribution is broader at positive latitudes than at negative latitudes, likely reflecting the bias towards more detections in the north. Furthermore, the SNR curves are broader than both the fiducial models, and therefore the observed SNR slope near  $\ell = 0$  is shallower. This could reflect the bias against SNR detection in the central regions of the Galactic plane due to crowding. Intriguingly, the <sup>26</sup>Al-based distribution agrees better with the SNR data, providing a particularly good match for the positive latitude data. Thus the observed SNR latitude and longitude distributions favor different models, though biases are likely to influence the comparison.

Finally, the bottom panel of 8 shows the cumulative longitude distribution of the naked-eye supernovae. Here the CCSN and <sup>26</sup>Al-based models give similar results and are much broader than the SNIa case. The historical supernovae of both types depart significantly from all of the predictions. As expected, this is driven by the events at large  $\ell$  that are not predicted in any of the models. We thus conclude that difficulty in explaining these outer-quadrant events is a quite general feature of our models. This suggests that the solution will require we relax one or more of our basic assumptions, as we will discuss more below.

#### 4.4 Historic Events and Milky-Way Supernova Rates

Our model predicts the fraction of all events that are visible to the naked eye. This corresponds to an integral of the sky density as in eq. (8), but the Monte Carlo approach is particularly useful for this calculation. For both CCSN and SNIa, we create a realization of 30,000 events, and ask what fraction are visible from the Sun's location, as a function of the limiting magnitude  $m_{V,lim}$ . Results appear in Fig. 12, with the solid curves using the sustained luminosity of  $M_V(90 \text{ days})$  as in Table 2. At  $m_{V,lim} = 2$  we find  $(f_{vis,CC}, f_{vis,Ia}) = (0.33, 0.13)$ , in good agreement with our results from the direct integration method. The upper and lower bands around each curve correspond to the results for the sustained luminosity at  $\Delta t = 30 \text{ days}$  and  $90 \text{ days}$ , respectively.

Figure 12 shows that for both SN types, the observability drops as we demand a brighter limiting magnitude; this is as expected. The SNIa fraction is higher because more events occur out of the midplane. Around  $m_{V,lim} \sim 1$ , the SNIa probability converges down to the CCSN probability. This reflects the fact that such bright events must occur so nearby that extinction becomes unimportant. In this

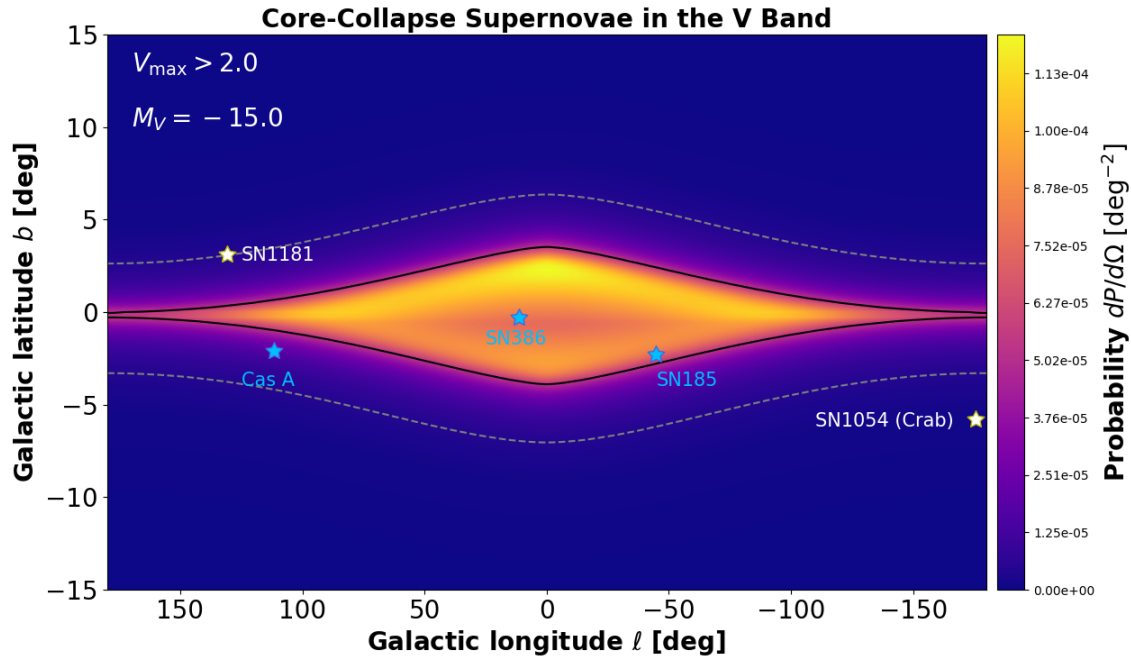


**Figure 9.** Sky plot of the probability density for core-collapse supernovae observed at Earth with apparent magnitude  $m_V \geq 2$  mag. The coordinates and stretched vertical axis are as in Figs. 2 and 3. Effects of dust extinction is taken into account, and the supernova absolute magnitude is taken to be  $M_V = -15$ , representative of the 90 day sustained CCSN luminosities in Table 2. Confirmed historical CCSNe are shown in white stars, possible historical events are shown as shaded stars. The all-sky probability integrates to  $P_{CC,tot} = 14\%$  of all CCSN are visible to the naked eye; the black (gray) contour encloses 68% (95%) of this total probability.

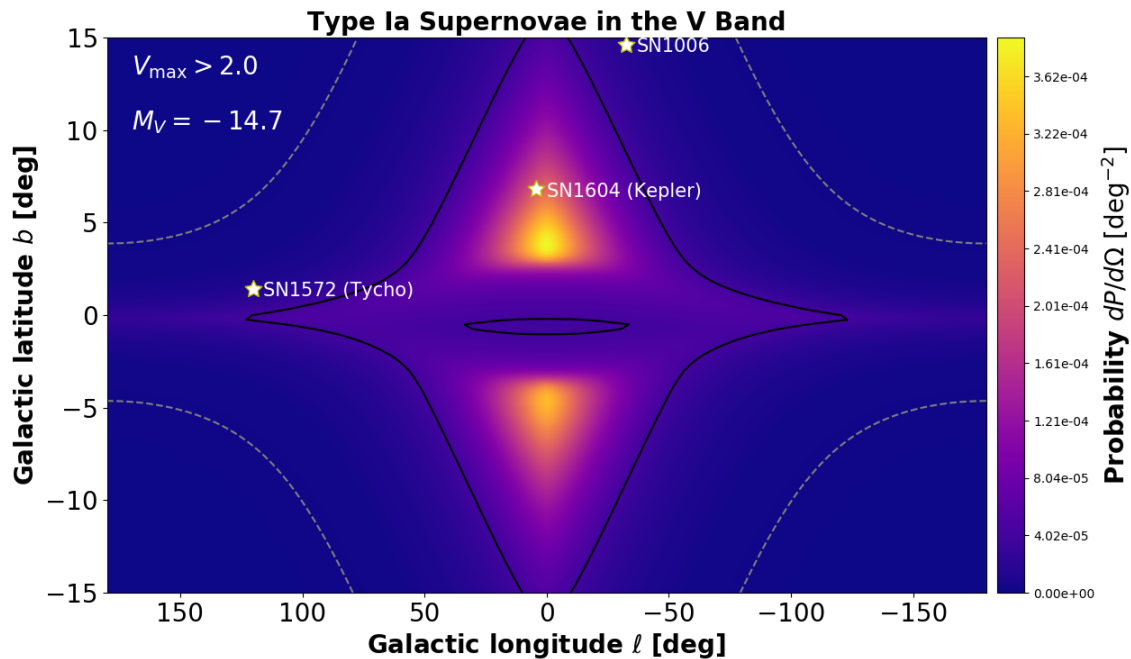


**Figure 10.** Events brighter than  $m_V = 2$  as in Fig. 9, but for Type Ia supernovae, taken to have absolute magnitude  $M_V = -14.7$  corresponding to the 90 day sustained luminosity in Table 2. The all-sky probability integrates to  $P_{Ia,tot} = 33\%$  of all SNIa are visible to the naked eye; the black (gray) contour encloses 68% (95%) of this total probability.

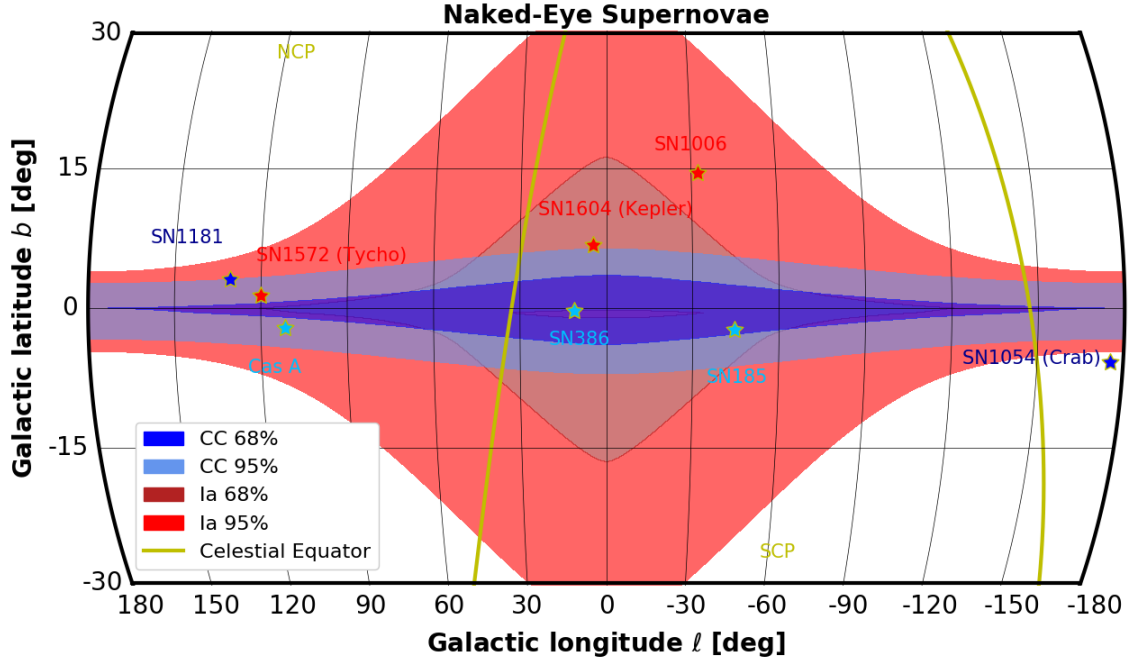


**Figure 11.** Zoom-out map in Galactic coordinates of naked-eye supernova probability density similar to Fig. 4. Visible probability density show for CCSN as in Fig. 9 and Type Ia events as in Fig. 10. Historical supernovae are labeled as in Fig. 4; we see that the confirmed historical events avoid the far southern sky, likely reflecting the lack of available information from civilizations in the southern hemisphere.

limit, the fraction just corresponds to the small probability of having very nearby events around the solar location. The bands around the curves illustrate that the results are quite sensitive to the duration required for supernova discovery. Type Ia events show particularly strong variations, reflecting their strong drop in luminosity at late times.

Figure 13 also shows the fraction of supernova visibility versus apparent magnitude, now for a wide range of supernova absolute magnitudes. This allows for estimation of the observability at any point along the light curve. For example, from Table 2 we see that Type II-P supernovae have  $M_V = -17.0$  mag at peak but a sustained luminosity of  $M_V(180 \text{ days}) = -13.9$  mag. From the top panel of Fig. 13 we see that at  $m_{V,\text{lim}}^{\text{SN}} = 2$  mag, these magnitudes correspond to detection probabilities of about 20% and 6% respectively. This illustrates the importance of the timescale needed for supernova discovery and confirmation.

We can use historical supernova observations, along with our observable fractions, to estimate the underlying global Milky Way supernova rates. For supernova type  $i$ , the expected number  $N_{\text{obs}}$  of events observed over a duration  $\Delta t_{\text{obs}}$

$$N_{\text{obs}} = f_{\text{vis}} f_{\text{night}} \mathcal{R}_i \Delta t_{\text{obs}} \quad (21)$$

Note that any given region of the sky is not observable for 6 months because it is up during the day. To account for this we assign a fraction  $f_{\text{night}} \approx 1/2$  of events that occur at night. Thus we can estimate the global rate as

$$R_i = \frac{N_{i,\text{obs}}}{f_{\text{vis},i} f_{\text{night}} \Delta t_{\text{obs}}} \quad (22)$$

Of course the uncertainties are considerable due to the small number of events, and so this exercise is best seen as a consistency check of

our model. Using the historical data  $(N_{\text{obs,Ia}}, N_{\text{obs,II}}) = (3, 2)$  over  $\Delta t = 1$  kyr, we estimate

$$\mathcal{R}_{\text{Ia}} = 1.8_{-1.2}^{+1.4} \left( \frac{0.33}{f_{\text{vis,Ia}}} \right) \text{ events/century} \quad (23)$$

$$\mathcal{R}_{\text{CC}} = 3.1_{-1.9}^{+3.5} \left( \frac{0.15}{f_{\text{vis,CC}}} \right) \text{ events/century} \quad (24)$$

where the errors account only for Poisson counting statistics (Feldman & Cousins 1998). These are in good agreement with estimates in Table 1 from the compilation in Adams, et al. (2013); which performed a similar (but not identical) analysis using the same historical supernovae. Our result is thus also consistent within errors with the Rozwadowska, Vissani, & Cappellaro (2021) global mean of supernova rate estimators, though at the high end of their range, as is typical of estimates base on rates inferred from the solar neighborhood (e.g., van den Bergh 1990; Dragicovich, Blair & Burman 1999; Reed 2005).

Finally, Fig. 12 invites us to consider the implications for the next Galactic supernova for naked-eye stargazers. Based on the intrinsic rates in Fig. 1, a CCSN is the most likely next event. We see that even at nominal human detection limit  $m_{V,\text{lim}} \approx 6$ , there is only about a 1 in 3 chance that such an event will be visible to the naked eye. A brighter event is even less likely. For the next SNIa, there is more hope. The odds are about 1 in 2 that it will be at the threshold of human vision. And the odds remain as high as about 1 in 3 that it will attain a sustained apparent brightness of at least  $m_V = 2$  for 90 days, which would provide a memorable sight.

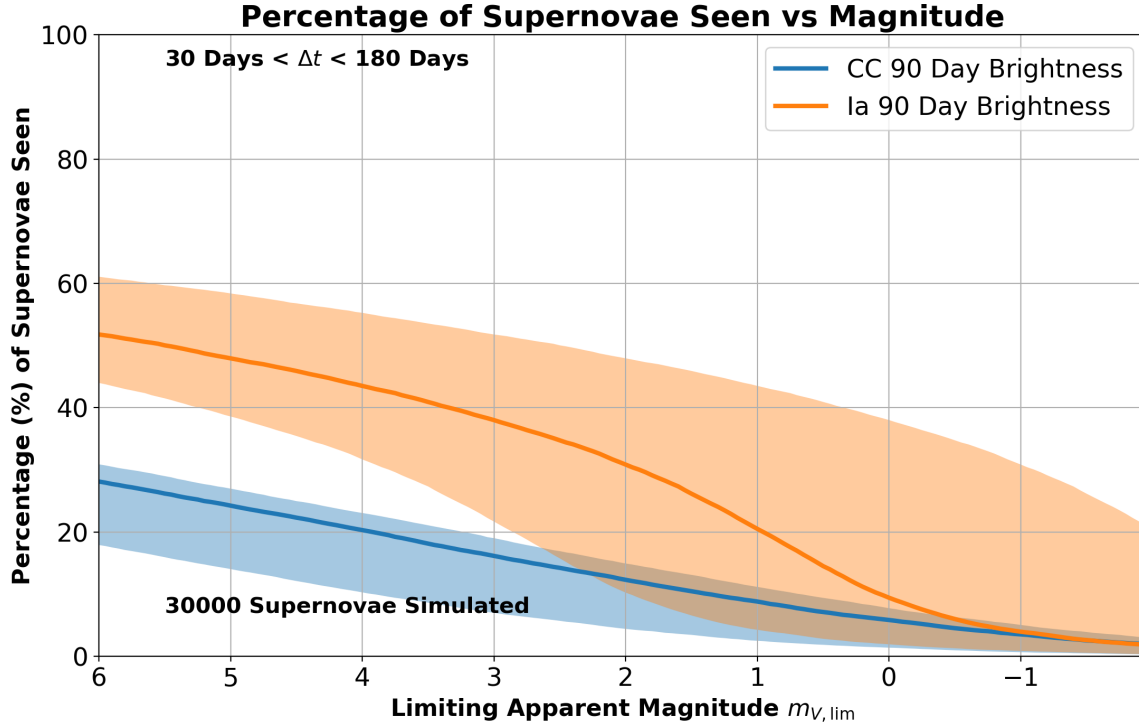


**Figure 12.** Plot of percentage of both types of supernovae seen for limiting magnitudes  $m_{V,lim}$  set to different sustained luminosities  $M_V$  ( $\Delta t$ ). Solid curves are for  $\Delta t = 90$  days, upper (lower) band is for  $\Delta t = 30$  (180) days. Orange curves are for Type Ia events, and blue curves are for CCSN.

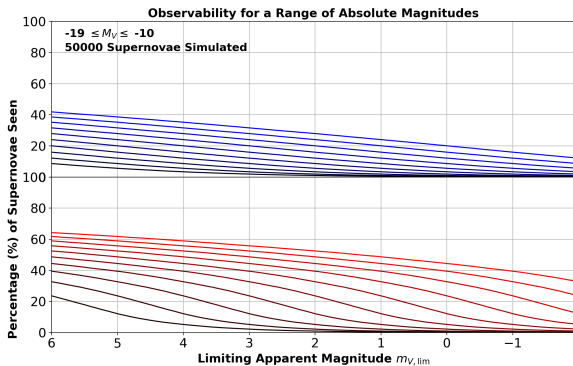


**Figure 13.** Fractions of supernovae visible as naked-eye events, plotted as a function of apparent magnitude as in Fig. 12; *top panel*: CCSN, *bottom panel*: SNIa. Shown for both supernova types, and for 10 values of absolute magnitude  $M_V = (-19, -18, \dots, -11, -10)$  going from top to bottom.

## 5 DISCUSSION

Despite the relatively small numbers of historical supernovae, their observed sky positions and time history give surprising insights into our model for naked-eye events. We have shown that historical (naked-eye) supernova sky positions largely avoid the peaks of the probability distributions we predict. This is acutely striking in the case of core-collapse events, where SN 1181 and the Crab that both lie in the outer Galactic quadrants near the anticenter, both in regions

that are low-probability for *any* of the axisymmetric exponential disk models we have considered. On the other hand putative locations of SN 185 and especially SN 386 are in regions our model favors. For historical Type Ia events the match is somewhat better, yet here too there are no events in the predicted highest probability regions.

This mismatch between predictions and historical observations is likely real and implies that our model is incomplete or incorrect. The patterns our model fails to capture are (1) an excess of events away from the central regions of the Galaxy, (2) an excess of events at relatively high latitude, and (3) a deficit of events near the Galactic center. These patterns suggest several possible solutions.

One possibility is that our assumption of axisymmetry has omitted important structures in the stellar or dust distributions. In this paper, we adopt an axisymmetric model of the Galaxy. This ignores the existence of spiral arms and assumes the disk is smooth. But observations of extragalactic supernovae confirm that core-collapse events are correlated with spiral arms, and that Type Ia events are as well, albeit more weakly (e.g., [Aramyan, et al. 2016](#)). Models for the Galactic pulsar distribution also favor compact object birth in spiral arms ([Faucher-Giguère & Kaspi 2006](#)). Indeed, [Dragicevich, Blair & Burman \(1999\)](#) suggest that supernova concentration in spiral arms leads to an anomalously high supernova rate near the Sun’s location in the Galaxy, and thus a higher Galactic rate using historical data than from other methods. Conversely, [Li, et al. \(1991\)](#) studied the observed Milky-Way supernova remnant distribution available at the time, and did not find a statistically significant association with spiral arms, though they suggest the observational bias might obscure such a correlation. Finally, we note that [Fujimoto et al. \(2020\)](#) study the

likelihood of stars located in regions near supernova explosions and note that these are most likely just outside spiral arms.

The historical events themselves seem to show an affinity for spiral arms. The Crab is found in the Perseus spiral arm, near the point in arm that is closest to the Sun. SN 1181 also lies in the Perseus arm, and Cas A may as well. SN 185 and SN 1006 may lie in or near the Sagittarius arm. Clearly, models with spiral structure merit investigation, and we plan to do so in future work.

It is striking that our global supernova rate estimates are in reasonable agreement with other methods, yet our sky distributions are generally poor matches for the locations of historical supernovae. This could be a coincidence, or it could suggest that our model reasonably captures the the statistics of supernova obscuration while not accounting for local departures from axisymmetry.

The lack of well-studied historical records from the southern hemisphere raises the question of whether there have been historic events in the south that are absent from northern records. Indeed, Fig. 12 shows that our predicted CCSN and SNIa peaks are in the southern hemisphere. Mitigating against this is the record of the confirmed and suspected historical supernovae. Of the five confident events, two were seen in the southern sky: SN 1604 and SN 1006. Notably, SN 1006 at  $-42^\circ$  is substantially further south than the Galactic center at  $-29^\circ$ . If we identify SN 185 with RCW 86, this would be discovery at  $-62.5^\circ$ , near the southernmost excursion of the Galactic plane. This seemingly demonstrates that at least some northern historical observers could have seen supernovae in and around the Galactic center.

Thus it is at least possible that there may be a true deficit of reported supernovae in this region where our predictions peak. A search for records in southern hemisphere civilizations (e.g., Hamacher 2014) would be invaluable to confirm this, to cover regions in the Galactic plane inaccessible from the north, and to potentially gain new information on known historical events.

Another effect we have ignored is that that stars are generally formed in clusters, and CCSN progenitors in particular are formed in OB associations. Our model ignores spatial clustering, implicitly assuming that supernova locations are uncorrelated. To include this effect, one could view our probability distribution as describing the locations of *clusters* rather than individual stars. Then as long as the statistics of stars within clusters does not vary across the Galaxy, then our predictions are unchanged. We also note that the clustered birth of massive stars would also lead to correlations of explosions in *time* as well as space, but on timescales  $\gtrsim 10^6$  yr associated with star formation. Thus we do not expect multiple events from the same cluster in the historic record.

Finally, we note that our formalism for supernova probability distributions invites other applications. One natural extension is to consider very nearby supernovae ( $\lesssim 100$  pc) that might deposit debris on Earth such as radioactive  $^{60}\text{Fe}$ , which has indeed been detected in terrestrial and lunar samples from an event  $\sim 3$  Myr ago, as reviewed in Fields et al. (2019). Sovgut et al. (2020) adapt our formalism to find the probability of nearby events as a function of distance. This updates earlier work going back to Shklovsky (1968), and including the lively Hartmann, Kretschmer, & Diehl (2002) study of supernova and gamma-ray burst “disturbance ecology,” which takes into account the effects of the vertical profiles of the events themselves as well as Galactic dust.

## 6 CONCLUSIONS

We summarize our results as follows:

- We have developed expressions to calculate the probability distribution on the sky for supernovae of different types, allowing for dust effects and an observer flux limit. We implement this formalism in the case of axisymmetric models of the Milky Way SNe and dust spatial distributions. Our fiducial model is that of Adams, et al. (2013), itself based on the TRILEGAL model for the thin and thick disks.
- We present the intrinsic probability distributions on the sky for both CCSN and SNIa, ignoring the effects of dust obscuration and optical flux limit. As expected, for both supernova types, the probable regions are along the Galactic plane and concentrated in the central Galactic quadrants, with peaks near the Galactic center. The thick-disk component of SNIa has a larger scale height and slightly smaller scale radius than the thin-disk that hosts CCSN, lead to a SNIa distribution that stretches to larger latitudes but a slightly more narrow longitude range.
- To model naked-eye events that comprise the historical SNe, we introduce a “sustained luminosity” observability criterion to account for the necessity of repeated observations to confirm supernovae as worthy of historical note. Table 2 shows how the various SN types dim over time, and that the types that are initially brighter may end up becoming dimmer than other types on the same timescale.
- We present sky maps of CCSN and SNIa probabilities. Our models predict the intrinsic, underlying distribution of both to most probable near the Galactic center, and both are found at long the Galactic plane, CCSN at low latitudes and SNIa extending to higher latitudes. For naked-eye events in the presence of dust extinction, the distributions still peak near the Galactic center and at relatively low latitudes.
- We compare our models with confirmed and likely historic supernovae. The confirmed events all *avoid* the high-probability regions of our fiducial models for both CCSN and SNIa; indeed the Crab is at high latitudes nearly at the anticenter. We conjecture that spiral arm effects can be important here and we are investigating this.
- Using our model we calculate the fraction of Galactic events visible to the naked eye, and use historical events to estimate Galactic rates, finding good agreement with other methods.
- As a contrast to our fiducial model based on stellar disk populations, we present results for supernovae following the much more diffuse spatial distribution inferred from  $^{26}\text{Al}$  sky maps. We find that these sky maps are broader than our fiducial results in both longitude; while the longitude distribution is broadly consistent with the observed supernova remnant, the predicted latitude distribution is substantially broader. Also, even in this case, the highest latitude historic events are not well explained.
- Assuming a limiting visible magnitude of 2 over  $\Delta t = 90$  days, we evaluate the chances of naked-eye visibility of the next Galactic supernova. At the  $m_V = 6$  limit, we find about a 33% chance of seeing the next CCSN and about a 50% chance of seeing the next SNIa.

There remains ample opportunity for future work. We plan to relax the assumption of axisymmetry, examining the effect of spiral arms in the predicted event maps. We encourage a search for indications of supernovae and other transients in historical records from the southern hemisphere. Finally, we look forward to deep surveys of the southern sky in the radio by the Square Kilometer Array and in high-energy gamma rays by the Cerenkov Telescope Array; this may detect the expansion of Galactic supernova remnants, and reveal new remnants, perhaps including events within the historical past (Ingallinera et al. 2017).

**ACKNOWLEDGEMENTS**

It is a pleasure to acknowledge many useful discussions with Ashvini Krishnan, Danny Milisavljevic, Paul Ricker, Danylo Sovgut, Alexandra Trauth, and Xilu Wang. BDF gratefully acknowledges fruitful discussions with all of the participants of the “Historical Supernovae, Novae, and Other Transients” workshop held in Oct. 2019, and the Lorentz Center at the University of Leiden for their hospitality in hosting this event. An earlier version of this paper was submitted by JWH as a Senior Thesis to the Department of Astronomy at the University of Illinois.

This work uses ADS extensively, and used the Python packages Matplotlib (Hunter 2007), NumPy (Oliphant 2006), SciPy (Jones et al. 2001), and AstroPy (Astropy Collaboration et al. 2013).

**REFERENCES**

- Abbott B. P., Abbott R., Abbott T. D., Abraham S., Acernese F., Ackley K., Adams C., et al., 2020, *PhRvD*, 101, 084002
- Adams S. M., Kochanek C. S., Beacom J. F., Vagins M. R., Stanek K. Z., 2013, *ApJ*, 778, 164
- Al Kharusi S., BenZvi S. Y., Bobowski J. S., Brdar V., Brunner T., Caden E., Clark M., et al., 2020, arXiv, arXiv:2011.00035
- Antonoli P., et al., 2004, *NJPh*, 6, 114
- Aramyan L. S., et al., 2016, *MNRAS*, 459, 3130
- Astropy Collaboration, Robitaille T. P., Tollerud E. J., Greenfield P., Droettboom M., Bray E., Aldcroft T., et al., 2013, *A&A*, 558, A33. doi:10.1051/0004-6361/201322068
- Bartunov O. S., Tsvetkov D. Y., Pavlyuk N. N., 2007, *HiA*, 14, 316
- Bianco F. B., Modjaz M., Hicken M., Friedman A., Kirshner R. P., Bloom J. S., Challis P., et al., 2014, *ApJS*, 213, 19
- Bortle J. E., 2001, *Sky and Telescope*, 101, 126
- Brown P. J., Breeveld A. A., Holland S., Kuin P., Pritchard T., 2014, *Ap&SS*, 354, 89
- Cinzano P., Falchi F., Elvidge C. D., 2001, *MNRAS*, 323, 34
- Clark D. H., Stephenson F. R., 1977, *The Historical Supernovae*, Pergamon Press, Oxford
- Clark R. N., 1990, *Visual Astronomy of the Deep Sky*, Cambridge: Cambridge University Press
- Dall’Ora M., Botticella M. T., Pumo M. L., Zampieri L., Tomasella L., Pignata G., Bayless A. J., et al., 2014, *ApJ*, 787, 139
- de Jaeger T., Zheng W., Stahl B. E., Filippenko A. V., Brink T. G., Bigley A., Blanchard K., et al., 2019, *MNRAS*, 490, 2799
- Doherty C. L., Gil-Pons P., Lau H. H. B., Lattanzio J. C., Siess L., 2014, *MNRAS*, 437, 195. doi:10.1093/mnras/stt1877
- Dragicevich P. M., Blair D. G., Burman R. R., 1999, *MNRAS*, 302, 693
- DUNE collaboration, Abi B., Acciarri R., Acero M. A., Adamov G., Adams D., Adinolfi M., et al., 2020, arXiv, arXiv:2008.06647
- Faucher-Giguère C.-A., Kaspi V. M., 2006, *ApJ*, 643, 332
- Feldman G. J., Cousins R. D., 1998, *PhRvD*, 57, 3873
- Fesen R. A., Hammell M. C., Morse J., Chevalier R. A., Borkowski K. J., Dopita M. A., Gerardy C. L., et al., 2006, *ApJ*, 645, 283
- Fields B., Ellis J. R., Binns W. R., Breitschwerdt D., deNolfo G. A., Diehl R., Dwarkadas V. V., et al., 2019, *BAAS*, 51, 410
- Fujimoto Y., Krumholz M. R., Inutsuka S.-. ichiro., Boss A. P., Nittler L. R., 2020, *MNRAS*, 498, 5532. doi:10.1093/mnras/staa2778
- Fujimoto Y., Krumholz M. R., Inutsuka S.-. ichiro., 2020, *MNRAS*, 497, 2442. doi:10.1093/mnras/staa2125
- Girardi L., Groenewegen M. A. T., Hatziminaoglou E., da Costa L., 2005, *A&A*, 436, 895
- Green D. A., 2015, *MNRAS*, 454, 1517
- Green D. A., 2017, in *Handbook of Supernovae*, A. W. Alsabti and P. Murdin eds, Springer, p 37
- Green D. A., 2019, *JApA*, 40, 36
- Green D. A., Gull S. F., 1984, *Nature*, 312, 527
- Green D. A., Stephenson F. R., 2017, in *Handbook of Supernovae*, A. W. Alsabti and P. Murdin eds, Springer, p 179
- Green G. M., Schlafly E. F., Finkbeiner D. P., Jurić M., Rix H.-W., Burgett W., Chambers K. C., et al., 2014, *ApJ*, 783, 114. doi:10.1088/0004-637X/783/2/114
- Green G. M., Schlafly E., Zucker C., Speagle J. S., Finkbeiner D., 2019, *ApJ*, 887, 93. doi:10.3847/1538-4357/ab5362
- Guillochon J., Parrent J., Kelley L. Z., Margutti R., 2017, *ApJ*, 835, 64
- Hamacher D. W., 2014, *JAHH*, 17, 161
- Hartmann D. H., Kretschmer K., Diehl R., 2002, *nuas.conf*, 154
- Hunter J. D., 2007, *CSE*, 9, 90. doi:10.1109/MCSE.2007.55
- Ikedo M., Takeda A., Fukuda Y., Vagins M. R., Abe K., Iida T., Ishihara K., et al., 2007, *ApJ*, 669, 519
- Ingallinera A., Triglio C., Umana G., Leto P., Buemi C., Schillirò F., Bufano F., et al., 2017, *IAUS*, 331, 345. doi:10.1017/S1743921317004574
- Jones E., et al., 2001, *SciPy: Open Source Scientific Tools for Python*. Available at: <http://www.scipy.org/>
- Katsuda, S., 2017, in *Handbook of Supernovae*, A. W. Alsabti and P. Murdin eds, Springer, p 63
- Kelly P. L., Kirshner R. P., 2012, *ApJ*, 759, 107. doi:10.1088/0004-637X/759/2/107
- Kelly P. L., Kirshner R. P., Pahre M., 2008, *ApJ*, 687, 1201. doi:10.1086/591925
- Kepler J, 1606, *De Stella Nova in Pede Serpentarii*, Paul Sessius, Praha, Czech Republic, Available online: [https://www.univie.ac.at/hwastro/rare/1606\\_kepler.htm](https://www.univie.ac.at/hwastro/rare/1606_kepler.htm)
- Kothes R., 2013, *A&A*, 560, A18
- Krause M. G. H., Rodgers-Lee D., Dale J. E., Diehl R., Kobayashi C., 2020, arXiv, arXiv:2011.08615
- Krause O., Tanaka M., Usuda T., Hattori T., Goto M., Birkmann S., Nomoto K., 2008, *Natur*, 456, 617
- Kunkel W., Madore B., Shelton I., Duhalde O., Bateson F. M., Jones A., Moreno B., et al., 1987, *IAUC*, 4316
- Li Z., Wheeler J. C., Bash F. N., Jefferys W. H., 1991, *ApJ*, 378, 93
- Li, W., Leaman, J., Chornock, R., et al. 2011, *MNRAS*, 412, 1441
- Luken K. J., et al., 2019, *MNRAS.tmp*, 3072
- Mauerhan J. C., Smith N., Silverman J. M., Filippenko A. V., Morgan A. N., Cenko S. B., Ganeshalingam M., et al., 2013, *MNRAS*, 431, 2599
- Munari U., Henden A., Belligoli R., Castellani F., Cherini G., Righetti G. L., Vagnozzi A., 2013, *NewA*, 20, 30
- Novoseltsev Y. F., Boliev M. M., Dzaparova I. M., Kochkarov M. M., Kurenya A. N., Novoseltseva R. V., Petkov V. B., et al., 2020, *APH*, 117, 102404
- Oliphant, T., 2006, *A Guide to NumPy*, Trelgol Publishing, USA
- Prentice S. J., Ashall C., Mazzali P. A., Zhang J.-J., James P. A., Wang X.-F., Vinkó J., et al., 2018, *MNRAS*, 478, 4162
- Reed B. C., 2005, *AJ*, 130, 1652
- Reynolds S. P., Borkowski K. J., Green D. A., Hwang U., Harrus I., Petre R., 2008, *ApJL*, 680, L41
- Rozwadowska K., Vissani F., Cappellaro E., 2021, *NewA*, 83, 101498
- Sahu D. K., Anupama G. C., Chakradhari N. K., 2013, *MNRAS*, 433, 2
- Schlafly E. F., Finkbeiner D. P., 2011, *ApJ*, 737, 103. doi:10.1088/0004-637X/737/2/103
- Schlafly E. F., Finkbeiner D. P., Schlegel D. J., Jurić M., Ivezić Ž., Gibson R. R., Knapp G. R., et al., 2010, *ApJ*, 725, 1175. doi:10.1088/0004-637X/725/1/1175
- Schlegel D. J., Finkbeiner D. P., Davis M., 1998, *ApJ*, 500, 525. doi:10.1086/305772
- Scholberg K., 2012, *ARNPS*, 62, 81
- Shivvers I., et al., 2017, *MNRAS*, 471, 4381
- Shklovsky I. S., 1968, *Supernovae, Interscience Monographs and Texts in Physics and Astronomy Vol. XXI*, Wiley
- Smith N., 2013, *MNRAS*, 434, 102
- Sovgut, D., Krishnan, A., Trauth, A., Fields, B. D., 2020, in preparation
- Stahl B. E., Zheng W., de Jaeger T., Filippenko A. V., Bigley A., Blanchard K., Blanchard P. K., et al., 2019, *MNRAS*, 490, 3882
- Stephenson F. R., Green D. A., 2002, *Historical Supernovae and Their Remnants*, Oxford University Press, Oxford
- Stephenson F. R., Green D. A., 2005, *JHA*, 36, 217



Stephenson F. R., Green D. A., 2009, JHA, 40, 31  
 Strader J., et al., 2018, arXiv, arXiv:1811.12433  
 van den Bergh S., 1990, AJ, 99, 843  
 van den Bergh S., Dodd W. W., 1970, ApJ, 162, 485  
 Vink J., Bleeker J., van der Heyden K., Bykov A., Bamba A., Yamazaki R., 2006, ApJL, 648, L33  
 Vink J., Kaastra J. S., Bleeker J. A. M., 1997, A&A, 328, 628  
 Vink, J., 2017, in Handbook of Supernovae, A. W. Alsabti and P. Murdin eds, Springer, p 139  
 Wang W., Siebert T., Dai Z. G., Diehl R., Greiner J., Heger A., Krause M., et al., 2020, ApJ, 889, 169. doi:10.3847/1538-4357/ab6336  
 Wang X., Fields B. D., Lien A. Y., 2019, MNRAS, 486, 2910

## APPENDIX A: SOLVING SIGHTLINE DISTANCE TO A FIXED LIMITING MAGNITUDE

To compute and map supernova probability to an observed depth  $m_{V,\text{lim}}^{\text{SN}}$ , for each sightline we need to find the distance  $r$  that satisfies

$$m_V(r) = m_{V,\text{lim}}^{\text{SN}} \quad (\text{A1})$$

where  $m_V$  is given by eq. (13). This is the distance at which a supernova of a given absolute magnitude has the threshold apparent magnitude in the presence of extinction. The need to evaluate the extinction via a numerical integral prevents an analytic solution.

This equation can be efficiently solved via root finding. Specifically, we use Newton's method to iteratively find the root of  $f(r) = m_V(r) - m_{V,\text{lim}}^{\text{SN}}$ , which has derivative

$$f'(r) = \mu'(r) + A'_V(r) \quad (\text{A2})$$

$$\mu'(r) = \frac{1}{r \ln 10} \quad (\text{A3})$$

$$A'_V(r) = \kappa_V \rho_{\text{dust}}(r). \quad (\text{A4})$$

The method benefits from the fact that  $f'$  is simply a function evaluation, while  $f$  requires numerical integration. Generally we find that the solution converges after a few iterations.

## APPENDIX B: MONTE CARLO POPULATION

Using a Monte Carlo randomization technique we were able to randomly populate the Milky Way with SNE following the TRILEGAL model of stellar distribution by assigning a random position of cylindrical radius, height, and angle drawn from our adopted rate density function for that SN type. The angle is drawn from a uniform distribution  $\theta \in [0, 2\pi]$ , and the height  $z$  is drawn (with both signs) from an appropriate exponential distribution in  $z/h_i$  for disk component  $i$ . The radial distribution is slightly more involved: the cumulative (volume-integrated) probability is

$$P(< R) = \frac{1}{R_i^2} \int_0^R e^{-R'/R_i} R' dR' = 1 - e^{-x} (x + 1) \quad (\text{B1})$$

where  $x = R/R_i$ . Thus given a uniform random variable  $u$ , the radius is found by solving for

$$x = \ln \frac{x + 1}{1 - u} \quad (\text{B2})$$

Since it is impossible to isolate  $x$  in this equation, we used a root finding technique to find  $x$  to a precision of 0.0001.

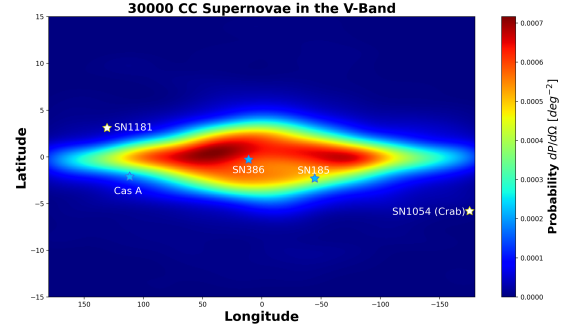


**Figure B1.** Probability map for naked-eye CCSNe, exactly as in Fig. 9 but calculated using our Monte Carlo method.

### B1 Conversion of Coordinates

The random generation of SNe in the Galaxy were generated with Galactocentric cylindrical coordinates  $(R, \theta, z)$ , but in order to calculate magnitude as viewed from the Earth these must be converted to solar-centered coordinates. The distance from the sun to the SN is calculated using:

$$r = \sqrt{(R \cos \theta - R_\odot)^2 + (R \sin \theta)^2 + (z - h_\odot)^2} \quad (\text{B3})$$

The Galactic longitude for points with  $R < R_\odot$  is:

$$\ell = \begin{cases} \arcsin\left(\frac{R \sin \theta}{r}\right), & R \cos \theta < R_\odot \\ \pi - \arcsin\left(\frac{R \sin \theta}{r}\right), & R \cos \theta > R_\odot. \end{cases} \quad (\text{B4})$$

The Galactic latitude can be found by:

$$b = \arcsin\left(\frac{z - z_\odot}{R}\right) \quad (\text{B5})$$

### B2 Visibility

Using the typical absolute magnitude of a SN, the Galactocentric radius of the Sun, and the extinction due to dust, we are able to calculate the apparent magnitude of the event at Earth. Comparing this magnitude to the minimum apparent magnitude for naked-eye discovery we are able to determine whether each randomly generated SN would be visible on Earth. Doing this calculation for thousands of SNe and then taking the ratio of visible SNe to total SNe generated, we are able to generate a predicted percentage of SNe that should be detected.

### B3 Smoothing

After the instances are sorted by their visibility, we then used SciPy's Gaussian kernel density estimation (KDE) function to convert the discrete events into a probability density function (PDF) for  $-15^\circ < b < 15^\circ$ . This allows the final model for the sky distribution of supernovae to not be overfit and to stay consistent between Monte Carlo runs.

### B4 Results: Sky Maps

We have produced Monte Carlo version of the sky probability distributions shown in the main text. In Fig. B1 we show the results for naked-eye CCSN, using 30,000 simulated supernovae. The physical situation is identical to that shown in Fig. 9, to which the Monte

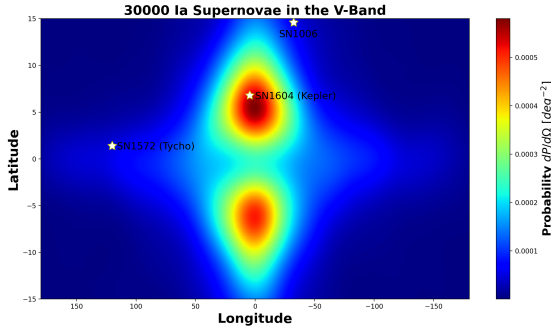


**Figure B2.** Monte Carlo calculation of the naked-eye SNIa sky distribution, exactly as in Fig. 10.

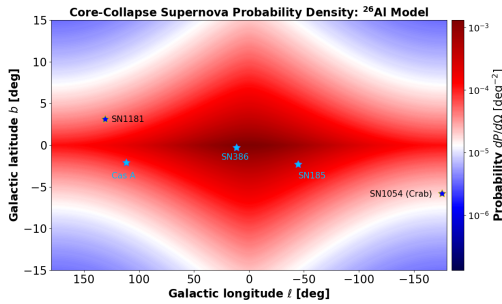


**Figure C1.** Intrinsic sky distribution of CCSN as in Fig. (2), but based on the observed  $^{26}\text{Al}$  sky distribution. The large scale radius and height leads to a more extended map both in latitude and longitude compared to our fiducial result seen in Fig. (2).

Carlo results should be compared. We see good agreement generally in the overall shape and amplitude. Note that while the integration method guarantees left-right symmetry, the Monte Carlo shows some fluctuations. We also see that the Monte Carlo version shows more smoothing, as expected. Finally, we see that the quantitative probability densities are in fair agreement, again with some differences due to smoothing.

Figure B2 shows our Monte Carlo results for 30,000 simulated SNIa, which should be compared to Fig. 10. Here again, the qualitative and quantitative agreements are good, though the Monte Carlo smoothing is evident as in Fig. B1.

### APPENDIX C: ALTERNATE SUPERNOVA DISTRIBUTION: ALUMINUM-26 SOURCES

To illustrate the impact of the adopted supernova distribution, here we show results for a case that represents an extreme deviation from the our fiducial Galactic model. As explained in §2, the supernova spatial distributions use thin and thick disk properties inferred from stellar counts in the TRILEGAL model (Girardi, et al. 2005). The supernova remnant distribution implies a similar scale radius (Green 2015). But the recent (Wang et al. 2020) analysis of the  $^{26}\text{Al}$  gamma-ray sky distribution is substantially broader, with a much larger scale radius and scale height (eq. 12). Insofar as  $^{26}\text{Al}$  nucleosynthesis is dominated by CCSN, this distribution would provide a direct measure of that population. We have therefore calculated the CCSN sky distribution using the  $^{26}\text{Al}$  disk parameters to give a feel for the

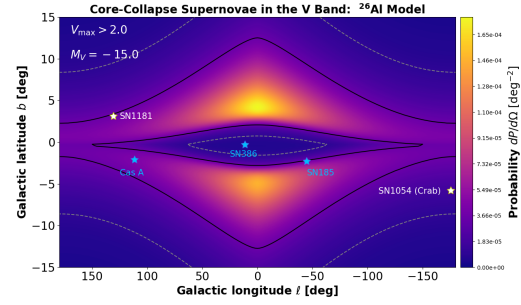


**Figure C2.** Naked-eye distribution of CCSN as in Fig. C2, but based on the  $^{26}\text{Al}$  sky distribution. Again we see a broader distribution in latitude and longitude, and a marked deficit in the central midplane regions.

sensitivity of our results to the disk parameters, and to explore the implications of the  $^{26}\text{Al}$  results. We retain the dust distribution in eq. (11), so that the dust is much more spatially compact than the supernovae themselves.

Figure C1 shows the intrinsic sky distribution of supernovae that follow the  $^{26}\text{Al}$  distribution. This is to be compared to the results from our fiducial case in Fig. 2; recall that these plots use a logarithmic scale for the probability density indicated by the color range. We see that the  $^{26}\text{Al}$  distribution has a wider span in Galactic longitude, and extends to higher latitudes. These are expected given the larger scale radius and height inferred from  $^{26}\text{Al}$ . While the Galactic center still has the maximum probability in the  $^{26}\text{Al}$  case, the peak value is lower than in the fiducial case. This reflects more diffuse nature of the  $^{26}\text{Al}$  map, and the requirement that the distribution is normalized to  $\int dP/d\Omega d\Omega = 1$ .

Figure C2 shows the sky distribution of naked-eye CCSN that follow the  $^{26}\text{Al}$  disk model. This is to be compared to the fiducial results in Fig. 9. The differences are dramatic. The peak regions are in the inner quadrants but at  $|b| \sim 5^\circ$  off of the plane. Also notable is a *deep minimum* in probability at and around the Galactic midplane. Both features are more extreme version of effects seen in our fiducial SNIa distribution in (Fig. 10, and trace back to similar causes. These reflect the more dilute supernova distribution in the  $^{26}\text{Al}$  picture: compared to the fiducial case, there are fewer supernovae along the midplane compared and more at larger heights. Thus, the more compact nature of the dust distribution leads to strong extinction at low latitudes but leaves the high latitudes unaffected.

Turning to the historical supernova locations in C2, we see that even in this model with supernovae extending to large radii and heights, still none of the supernovae lie in the peak regions. That said, the Crab, SN 1181, and Cas A lie in regions of higher probability than in Fig. 9, and the Crab is now inside the 95% contour. This reflects the high latitudes of these events. On the other hand, the low-latitude locations of SN185 and 386 are *disfavored* in this model, with SN 396 now outside of the 95% contour.

This paper has been typeset from a  $\text{\TeX}/\text{\LaTeX}$  file prepared by the author.